

1 **Bookshelf Kinematics and the Effect of Dilatation on Fault**  
2 **Zone Inelastic Deformation: Examples from Optical Image**  
3 **Correlation Measurements of the 2019 Ridgecrest**  
4 **Earthquake Sequence**

5  
6 Christopher Milliner<sup>1,2\*</sup>, Andrea Donnellan<sup>1</sup>, Saif Aati<sup>2</sup>, Jean-Philippe Avouac<sup>2</sup>, Robert Zinke<sup>1</sup>,  
7 James F. Dolan<sup>3</sup>, Kang Wang<sup>4</sup>, Roland Bürgmann<sup>4</sup>

8  
9 <sup>1</sup> *Jet Propulsion Laboratory, California Institute of Technology, Pasadena, CA*

10 <sup>2</sup> *California Institute of Technology, Pasadena, CA*

11 <sup>3</sup> *University of Southern California, Los Angeles, CA*

12 <sup>4</sup> *University of California, Berkeley, Berkeley, CA*

13 *\*corresponding author. milliner@caltech.edu*

14  
15  
16  
17 *This manuscript has been submitted for publication in Journal of Geophysical Research: Solid*  
18 *Earth. Please note that the peer-review is in progress, and subsequent versions of this*  
19 *manuscript may have different content. If accepted, the final version of this manuscript will be*  
20 *available via the ' Peer-reviewed publication DOI' link on the EarthArxiv webpage.*  
21  
22  
23  
24  
25  
26  
27  
28  
29  
30



62 **Abstract**

63

64 The 2019 Ridgecrest earthquake sequence initiated on July 4<sup>th</sup> with a series of foreshocks,  
65 including a  $M_w$  6.4 event, that culminated a day later with the  $M_w$  7.1 mainshock and resulted in  
66 rupture of a set of cross-faults. Here we use sub-pixel correlation of optical satellite imagery to  
67 measure the displacement, finite strain and rotation of the near-field coseismic deformation to  
68 understand the kinematics of strain release along the surface ruptures. We find the average off-  
69 fault deformation along the mainshock rupture is 34% and is significantly higher along the  
70 foreshock rupture (56%) suggesting it is a less structurally developed fault system. Measurements  
71 of the 2D dilatational strain along the mainshock rupture show a dependency of the width of  
72 inelastic strain with the degree of fault extension and contraction, indicating wider fault zones  
73 under extension than under shear. Measurements of the vorticity along the main, dextral rupture  
74 show that conjugate sinistral faults are embedded within zones of large clockwise rotations caused  
75 by the transition of strain beyond the tips of dextral faults leading to bookshelf kinematics. These  
76 rotations and bookshelf slip can explain why faults of different shear senses do not intersect one  
77 another and the occurrence of pervasive and mechanically unfavorable cross-faulting in this  
78 region. Understanding the causes for the variation of fault zone widths along surface ruptures has  
79 importance for reducing the epistemic uncertainty of probabilistic models of distributed rupture  
80 that will in turn provide more precise estimates of the hazard distributed rupture poses to nearby  
81 infrastructure.

82

83

84 **Keywords:** Ridgecrest, inelastic, off-fault deformation, finite strain, rotation, dilatation,  
85 distributed rupture

86

87

88

89 **1.1 Introduction**

90

91 The 2019 Ridgecrest earthquake sequence initiated on July 4<sup>th</sup> with a series of foreshocks that  
92 included a  $M_w$  6.4 event and culminated 34 hours later with a  $M_w$  7.1 mainshock event. This

93 sequence was also notable in that it resulted in rupture of a set of more than 20 cross-faults  
94 (Brandenberg et al., 2020; Ross et al., 2019; Xu et al., 2020). The earthquake sequence occurred  
95 within the northern region of the Eastern California Shear Zone (ECSZ), a 150-km-wide zone of  
96 NW-trending dextral shear that accommodates up to ~20% of the North America-Pacific plate  
97 boundary motion (McClusky et al., 2001; Rockwell et al., 2000). Seismic and geodetic inversions  
98 show the  $M_w$  6.4 event likely ruptured multiple fault segments, where it initiated on a short NW-  
99 trending, dextral fault, and then propagated to the southwest along a series of parallel NE-trending  
100 sinistral faults for 16 km (Liu et al., 2019; Ross et al., 2019; Chen et al., 2020; Goldberg et al.,  
101 2020; Wang et al., 2020). On July 5<sup>th</sup>, 34 hours after the foreshock, the  $M_w$  7.1 mainshock initiated  
102 ~15 km to the north, from where it propagated bilaterally at a relatively slow velocity of ~2 km/s  
103 along a NW-trending set of dextral faults for ~45 km. The mainshock rupture terminated at its  
104 northern extent within the Coso volcanic field and at its southern extent ~5 km from the Garlock  
105 fault, where it was found to have triggered creep at the surface along parts of the Garlock fault and  
106 a small cluster of seismicity (Barnhart et al., 2019; Ross et al., 2019). Field and remote-based  
107 mapping of geomorphic markers and vegetation lineaments indicate that both fault systems  
108 involved in the foreshock and mainshock show extensive evidence for faulting prior to their  
109 rupture in 2019 (Jobe et al., 2020), but their geologic fault slip rates currently remain unknown.  
110 The Ridgecrest sequence is also notable in that it occurred within a region of similar sized events,  
111 including the  $M_w$  ~7.5 1872 Owens Valley earthquake located ~45 km to the north, and the 1992  
112  $M_w$  7.3 Landers and 1999  $M_w$  7.1 Hector Mine earthquakes ~110 km to the south.

113

114 Here we use optical image correlation of satellite data to measure the near-field surface  
115 deformation patterns and study the kinematics of finite fault strain release along the Ridgecrest  
116 surface ruptures. Documenting coseismic surface strain is important as we describe in section 1.2,  
117 as it can alter the fault zone mechanical properties which are relevant to understanding earthquake  
118 dynamics and is an important input for constraining probabilistic models of distributed fault  
119 rupture hazard (e.g., Petersen et al., 2011). Here, we assess whether fault zones are wider and the  
120 strain distribution is different under tension and assess the effects of rotations adjacent to faults  
121 that may explain the occurrence of mechanically unfavorable cross-faulting. We also use our  
122 observations of surface strain to shed light on the regional scale tectonic questions of the Eastern  
123 California Shear Zone (ECSZ) and Garlock fault which we describe in the second section below.

124

125

## 1.2 Significance of distributed inelastic strain

126

127 Distributed inelastic strain is accommodated via a range of mechanisms across fault zones,  
128 including secondary fracturing, pervasive continuous shear and rotations (Shelef and Oskin, 2010).

129 These act to alter the mechanical properties of the fault zone material which in turn can affect a  
130 range of earthquake processes including the attenuation of seismic waves (Mitchell, 1995),

131 dissipation of rupture energy and velocity (Sammis et al., 2010; Dunham et al., 2011; Gabriel et  
132 al., 2013; Thomas and Bhat, 2018; Bao et al., 2019), and the ability of ruptures to fully reach the

133 surface (Kaneko and Fialko, 2011; Brooks et al., 2017). Therefore, understanding what controls

134 the variation of the magnitude, width and spatial decay of inelastic strain across fault zones has

135 importance for seismic hazard, both for accurately estimating the probability of seismic shaking

136 and distributed fault displacement (McGuire, 1995; Petersen et al., 2011). It is also important for

137 accurately estimating geologic fault slip rates that are susceptible to underestimating the long-term

138 displacement when restoring offset geomorphic features across fault zones (Dolan and Haravitch,

139 2014; Scharer et al., 2014).

140

141 Measurements of off-fault deformation (OFD) from field survey mapping and remote-based  
142 methods (e.g. lidar differencing and optical image correlation) of surface ruptures have shown that

143 the sediment thickness, type of near-surface material and fault dip have an important effect on the

144 amounts of off-fault distributed inelastic deformation (Rockwell et al., 2002; Dolan and Haravitch,

145 2014; Zinke et al., 2014; Gold et al., 2015; Teran et al., 2015; Milliner et al., 2015; 2016; Scott et

146 al., 2018; Zhou et al., 2018). However, how the distribution and magnitude of inelastic strain varies

147 in regions where the fault experiences fault-normal contraction and extension is less well

148 understood. This is largely due to the difficulty of measuring the fault-perpendicular component

149 of displacement in the field and the challenge of accurately estimating strain from geodetic

150 displacement measurements which requires sufficiently high-resolution sampling and low noise

151 when calculating the spatial derivatives. Here we analyze the surface deformation due to the 2019

152 Ridgecrest earthquakes for which such types of data exist. Specifically, we use these pixel tracking

153 of pre- and post-earthquake optical satellite imagery to evaluate the sensitivity of the width and

154 spatial attenuation of inelastic strain across the surface rupture to the amount of extension and  
155 contraction the fault zone experiences.

156

157 From our observations of the kinematics of surface strain we also seek to understand the  
158 widespread occurrence of orthogonal cross-faulting along the surface rupture. Cross-faulting  
159 occurred at almost all scales as shown by 100-m-long distributed fractures (Ponti et al., 2019; Xu  
160 et al., 2020), to the coseismic rupture strands involved directly in the foreshock-mainshock  
161 sequence and the distribution of aftershocks, which suggests cross-faulting is pervasive through  
162 the seismogenic crust and is not just a surficial feature (Ross et al., 2019). Similar cross-faulting  
163 rupture behavior has been observed during other large earthquakes (e.g., the 1987 Superstition  
164 Hills) and seems to be a common mode of strain release along the North American-Pacific plate  
165 boundary (Hudnut et al., 1989; Smith et al., 2020). Although the occurrence of faults with nearly  
166 orthogonal orientations is not uncommon, it is still poorly understood as the conventional Mohr-  
167 Coulomb faulting theory predicts that faults form at  $30^\circ$  from the direction of maximum  
168 compression and  $\sim 60^\circ$  from one another (Anderson, 1951). Here we attempt to understand why  
169 faults may occur in these mechanically unfavorable orientations relative to the background stress  
170 field by assessing the near-field kinematics along the Ridgecrest surface rupture at various scales  
171 which relate to different evolutionary stages of fault development.

172

173 We note that in our study we refer to the inelastic strain that is distributed across the fault zone and  
174 adjacent to the primary fault strand as off-fault deformation (OFD) and not as fault damage.  
175 Damage has been detected following major surface rupturing events by a decrease in the seismic  
176 velocity across the fault zone that is thought to occur by the generation of microcracks which  
177 reduces the rock's shear rigidity (Vidale and Li, 2003). Postseismically the seismic velocity of the  
178 damaged material has been found to recover and increase with time due to the closing and healing  
179 of microcracks, which indicates damage exhibits a time dependent behavior (Li et al., 2001).  
180 Damage can also be generated by the dynamic passing seismic waves with very little true shear  
181 strain in the form of shattered or "pulverized rocks" (Dor et al., 2006). In contrast the inelastic  
182 strain that we measure here is permanent, occurs at a much larger spatial and displacement scale  
183 (both  $> 10$  cm's) than microcracking and results from both the quasi-static and dynamic stresses.  
184 This suggests that in some cases damage and off-fault deformation reflect rock failure associated

185 with different processes and scales, and therefore here we do not use the two terms  
186 interchangeably.

187

### 188 **1.3 Regional Tectonics and outstanding questions**

189

190 Why the major faults in the ECSZ do not intersect or displace one another has been a long-standing  
191 problem because the kinematic evolution of fault junctions is not clear over long-term, geologic  
192 timescales. (Andrew and Walker, 2017; Frankel et al., 2008; Oskin and Iriondo, 2004; Oskin et al.,  
193 2008). For example, none of the major NW-trending dextral faults in the Mojave ECSZ (e.g., the  
194 Blackwater, Gravel Hills, North Lockhart and East Goldstone Lake faults, see Figure 1a and 6e)  
195 continue northward to intersect or displace the central Garlock fault (Andrew and Walker, 2017).  
196 The same can also be found at the southern margin of the Mojave Desert for the sinistral Pinto  
197 Mountain fault near the southern termination of the 1992 Landers rupture (Sieh et al., 1993).  
198 Numerical modeling and long-term geologic structural evidence indicate that dextral strain likely  
199 transitions to distributed off-fault deformation beyond fault tips (Andrew and Walker, 2017;  
200 Herbert et al., 2014). Paleomagnetic studies in this region have provided constraints of the rotation  
201 of panels of crustal blocks associated with regional-scale bookshelf faulting, finding rotations of  
202 up to  $\sim 40^\circ$  over the past  $\sim 10$  Ma (Schermer et al. 1996; Miller and Yount, 2002). However, there  
203 are an insufficient number of paleomagnetic measurements that constrain the spatial distribution  
204 and magnitude of rotations beyond the tips of NW-trending dextral faults to understand how the  
205 long-term elastic strain is released at the junctures with conjugate sinistral faults. Here, we seek to  
206 provide measurements of coseismic finite strain and rotations along the Ridgecrest rupture to  
207 understand how dextral shear strain may transition to rotation beyond fault tips and whether this  
208 can explain why the major conjugate faults in this region do not physically connect.

209

210 To answer the questions outlined above we used optical image correlation to, i) measure the 2D  
211 dilatational, shear and rotational components of horizontal strain across different transpressional  
212 and transtensional geometrical bends of the surface rupture and ii) asses how the width of the fault  
213 zone varies according to the magnitude of extension and contraction it experiences. To provide  
214 more robust estimates of how the inelastic strain decays as a function of distance from the primary  
215 fault trace we developed a template-based stacking method that minimizes smoothing of

216 displacement across the rupture, and we attempt to correct for the effect of smearing of the  
217 displacement signal caused by the convolution of the correlation window weighting function that  
218 arises during image matching. From the 2D displacement field we derive 2D finite strain maps and  
219 the infinitesimal vertical axis rotations to understand the kinematics of faulting along the rupture  
220 at the local and regional scale (10 and 100 km scale, respectively). We then use the strain and  
221 rotation maps to understand the mechanisms by which some faults in the ECSZ do not intersect or  
222 displace the Garlock fault, and the possible origin of cross-faulting and aftershock distributions  
223 given they are mechanically contradictory to conventional Mohr-Coulomb failure criteria.

224

## 225 **2. Data & Methods**

226

227 To measure the coseismic surface deformation we used subpixel image correlation of two optical  
228 SPOT-6 images that were acquired on September 15th, 2018 and July 24th, 2019 and therefore  
229 capture surface motion of both the foreshock and mainshock events. The SPOT images have a 60  
230 km footprint and resolution of 1.5 m, with almost the same incidence angles ( $9.57^\circ$  and  $9.55^\circ$  for  
231 the pre- and post-images respectively), which helps minimize topographic distortions that can arise  
232 from the parallax effect between different viewing geometries. To co-register, orthorectify and  
233 correlate the before and after images we used the COSI-Corr software (Leprince et al, 2007). The  
234 images are orthorectified using the satellite ancillary information which describes the exterior  
235 orientation (i.e., look angle, attitude and satellite position) and a 2 m pre-earthquake World-View  
236 DEM to correct for topographic distortions (Willis et al., 2019). The orthorectified and co-  
237 registered images were then correlated using COSI-Corr's phase correlator with a sliding window  
238 of  $32 \times 32$  pixels and step of 4 pixels, producing a disparity map of the horizontal surface  
239 displacement at 6 m resolution (Figure 1, see supplements S1 for details on noise of the result and  
240 image artifacts).

241

242 To measure the total fault-parallel offset and decay of inelastic fault-parallel shear strain across  
243 the surface rupture first requires projecting the 2D displacement maps (Figure 1) into the local  
244 fault-parallel direction and then stacking over the profile swath width to minimize the effect of  
245 noise. Here we have developed a new stacking profile method that provides a more accurate  
246 estimate of the distribution of fault-parallel surface motion across the rupture over standard profile



247 stacking approaches. Conventional stacking averages the fault-parallel motion along a constant  
 248 direction over the profile swath width. However, this can be problematic as it ignores variations  
 249 of the fault orientation within the profile swath that can lead to averaging of surface motion from  
 250 either side of the fault, which results in smoothing of the displacement distribution, artificial  
 251 widening of the fault zone and underestimation of the fault-parallel shear strains (see Figure S1  
 252 comparing conventional stacking versus our approach). To avoid this issue, we have developed a  
 253 subpixel template alignment stacking method, which first aligns each individual profile line with  
 254 subpixel precision prior to stacking. This is achieved by first creating a template from an initial  
 255 stack that is then cross-correlated with each individual profile line (here we use an along-fault  
 256 swath width of 138 m and across-fault profile length of 1-2 km, which includes 23 separate ‘profile  
 257 lines’). The optimal lateral shift to align each individual profile line is found with subpixel  
 258 precision by determining the peak of an outlier-resistant cross correlation coefficient. Once the  
 259 surface displacements are stacked with this approach, the total magnitude of the fault-parallel  
 260 offset (i.e., the total amplitude of the discontinuity shown in Figure S2 and S13) is then estimated  
 261 by inverting the fault-parallel displacements ( $y$ ), which are a function of the distance across the  
 262 profile ( $x$ ), for the coefficients of a linear and error function (eq. 1 and 2).

263

$$264 \quad y(x) = a + \frac{b}{2} \cdot \operatorname{erf}\left(\frac{x - c}{w_s \sqrt{2}}\right) + \varepsilon_{el} \cdot x \quad (1)$$

$$265 \quad \operatorname{erf}(z) = \frac{2}{\sqrt{\pi}} \int_0^z e^{-t^2} dt, \quad z = \frac{x - c}{w_s \sqrt{2}} \quad (2)$$

267

268 The parameters, which include the intercept ( $a$ ), total fault displacement ( $b$ ), fault location ( $c$ ), shear  
 269 width ( $w_s$ ) and slope ( $\varepsilon_{el}$ ), are estimated using a non-linear regression as  $c$  and  $w_s$  are nonlinear in the  
 270 model. The uncertainties for these are then estimated from the Jacobian, which contains the partial  
 271 derivatives of the residuals with respect to the model parameters, that is used to calculate the model  
 272 covariance matrix. The error function which characterizes the fault-parallel displacement across  
 273 the fault zone implies that the distribution of fault-parallel inelastic shear strain follows a Gaussian  
 274 distribution (i.e., the derivative of eq. 2), which is opposite in sign to the elastic strain. Therefore,  
 275 the variation of the fault-parallel shear strain ( $\varepsilon_{fp}$ , eq. [3]) across the fault zone can be expressed  
 276 as the summation of the inelastic strain ( $\varepsilon_{inel}$ ) and the fault-parallel elastic strain ( $\varepsilon_{el}$ , see Figure  
 277 S13), which is given by the following relation using the chain rule:

278

279

$$\varepsilon_{fp}(x) = \frac{dy(x)}{dx} = \frac{b}{w_s \sqrt{2\pi}} e^{-z^2} + \varepsilon_{el} \quad (3)$$

280

281

$$\varepsilon_{fp}(x) = \varepsilon_{inel} + \varepsilon_{el} \quad (4)$$

282

283

284

285

286

287

288

289

290

291

292

293

294

295

296

297

298

299

300

301

302

303

304

$$\frac{\Delta u_x(i, j)}{\Delta x} = \frac{u_x(i + 1, j) - u_x(i - 1, j)}{2\Delta x} \quad (5)$$

305

306

307

In the displacement profiles (eq. 1), the elastic strain in the near-field is approximated by a linear trend. We find this is reasonable given our profiles only sample the elastic dislocation signal within a short distance from the fault ( $\leq 1$  km) compared to the length scale at which the elastic signal varies, that follows  $\arctan(x)$  and is proportional to the depth extent of fault slip (Scholz [2019]), which for Ridgecrest is 10-15 km. In addition, other sources of noise such as satellite jitter and orbit artifacts affect surface motion at longer length scales ( $> 1$  km, see section S1) and therefore the estimated far-field gradient ( $\varepsilon_{el}$ ) from these displacement maps offers limited constraint of slip at seismogenic depths.

From the 2D displacement maps we calculate the finite surface strain and local infinitesimal rotations. We first apply a non-local means filter to reduce the effects of noise and then calculate the spatial gradients of the displacement field using a second-order accurate central difference approximation. Here we use the 2D displacement field  $u_d(i, j)$  that is the output of the image correlation (Figure 1), where subscript  $d$  is the change of position between the pre and post-event satellite images in the east-west direction (denoted by subscript  $x$ ) and north-south direction (denoted by subscript  $y$ ), where  $i, j$  denote the indices of the displacement field in the  $x$  and  $y$  axes and  $\Delta x$  is the displacement map resolution (6 m). For example, the gradient of the east-west component of displacement in the  $x$  direction is calculated using the following finite difference approximation:

Calculating the gradients of the displacement components ( $u_x, u_y$ ) in the  $x, y$  directions gives the displacement gradient tensor,  $\mathbf{D}$ ,

308

$$\mathbf{D} = \begin{bmatrix} \left(\frac{\Delta u_x}{\Delta x}\right) & \left(\frac{\Delta u_x}{\Delta y}\right) \\ \left(\frac{\Delta u_y}{\Delta x}\right) & \left(\frac{\Delta u_y}{\Delta y}\right) \end{bmatrix} \quad (6)$$

309 To calculate strain we use the Lagrangian finite strain tensor ( $\mathbf{E}$ ) instead of the typical infinitesimal  
 310 strain tensor because the condition of small strain is not met when resolving large strains across  
 311 the surface rupture (which can exceed 1% strain in most cases, see supplements where we show  
 312 the differences between the two strain approximations in Figure S2), and is calculated from the  
 313 following relation using Einstein summation convention,

(7)

314

$$\mathbf{E} = \begin{bmatrix} E_{xx} & E_{xy} \\ E_{yx} & E_{yy} \end{bmatrix}$$

315

$$E_{ij} = \frac{1}{2} \left( \frac{\Delta u_i}{\Delta x_j} + \frac{\Delta u_j}{\Delta x_i} + \frac{\Delta u_k}{\Delta x_i} \frac{\Delta u_k}{\Delta x_j} \right)$$

316

317 To measure contraction and extension along the rupture we calculate the dilatation (i.e., areal  
 318 strain) from the product of the principal stretches ( $1+E_i$ ,  $i = 1, 2$ ), where positive values denote  
 319 extension and negative values contraction (Ramsay, 1967). To illustrate areas with different senses  
 320 of shear and to measure the infinitesimal rotations of regions away from the faulting regions we  
 321 calculate the vorticity ( $\omega$ ) of the vector field, which is also defined as half the curl ( $c$ ).

322

$$\omega = \frac{c}{2} = \frac{1}{2} \left( \frac{\Delta u_x}{\Delta y} - \frac{\Delta u_y}{\Delta x} \right) \quad (8)$$

323 We note that the vorticity is used primarily to measure the amount of instantaneous local vertical  
 324 axis rotation of blocks away from faults (which has units of radians) or to illustrate the rotational  
 325 component of surface motion associated with simple shear strain but it does not measure the shear  
 326 strain component of simple shear (where  $\omega$  is defined as half the difference of the off-diagonal  
 327 components of the displacement gradient tensor [i.e., eq. 8] while the shear strain is the  
 328 summation). To help illustrate the variation of the total magnitude of strain along the surface  
 329 rupture we estimate the second invariant of the strain tensor ( $I_2$ ), which we call the total strain  
 330 intensity and can be computed from the determinant of  $\mathbf{E}$  or,

$$I_2 = \frac{1}{2}([\text{tr}(\mathbf{E})]^2 - \text{tr}[\mathbf{E}^2]) \quad (9)$$

The fault zone width is measured from each profile as the average width where the square root of  $I_2$  exceeds a threshold value of  $2 \times 10^{-3}$  which corresponds to 0.2% of the shear strain intensity and is an amount that corresponds to faulting observed in the field (Ponti et al., 2019; DuRoss et al., 2020).

### 3 Results

#### 3.1 Distribution of Inelastic Strain

The left-lateral slip distribution of the foreshock rupture shows a simple asymmetric triangular shape, while the right-lateral distribution of the mainshock is heterogeneous and multi-peaked (Figure 2b). These along-strike variations of slip at different length scales (from 1-10 km) are robust as indicated by the uncertainty in our measurements and may reflect variations due to the fault geometrical roughness and strength or applied stress (Dunham et al., 2011; Shi and Day, 2013; Milliner et al., 2016; Allam et al., 2019; Bruhat et al., 2020). These variations can provide useful constraints for the degree of aleatory variability of displacement along a rupture that inform scaling relations in probabilistic fault displacement hazard models (Lavrentiadis & Abrahamson, 2019). In addition, the total strain intensity map clearly shows changes of the total strain magnitude (Figure 3a), which correspond to variations of the fault geometry and orientation along the rupture. The total strain intensity is generally largest at the center of fault segments and systematically decreases towards their tips in areas of fault bends, branches or en-echelon steps. Along the foreshock rupture we find the mean and maximum left-lateral fault displacements of  $0.60 \pm 0.03$  m (all uncertainties represent 1 standard deviation error,  $1\sigma$ ) and  $1.40 \pm 0.07$  m ( $1\sigma$ ), respectively, and for the mainshock rupture the mean and maximum right-lateral displacements of  $1.69 \pm 0.06$  m ( $1\sigma$ ) and  $4.78 \pm 0.22$  m ( $1\sigma$ ), respectively (Table 1).

We estimate the magnitude of OFD along both ruptures as the percent of the total displacement that is not accommodated on the primary coseismic fault strand. OFD is estimated by subtracting the field observations ( $D_f$ ) (Ponti et al., 2019; DuRoss et al., 2020), which are assumed to capture the primary on-fault displacement, from the total displacement estimated by our optical stacked

361 profiles (which captures both the on- and off-fault deformation across the entire fault zone [ $D_o$ ])  
362 which is then normalized by  $D_o$ , i.e.,  $OFD = [(D_o - D_f)/D_o] \times 100$ . Normalizing the difference of  
363 the total and on-fault displacements (measured in meters) by  $D_o$ , allows for a more direct  
364 comparison of the amount of off-fault strain between the two ruptures which have different  
365 moment magnitudes and amounts of total slip. From this comparison we find OFD is largest near  
366 both terminations of the mainshock rupture (see Figure 2 for comparison and Figures S3 and S4)  
367 and is overall much larger for the foreshock (mean and median values of 56,  $65 \pm 15\%$ ,  $1\sigma$ ) than  
368 the mainshock (mean and median values of 34,  $25 \pm 15\%$ ,  $1\sigma$ ), which have negatively and  
369 positively skewed distributions, respectively (Figure S5). The foreshock and mainshock rupture  
370 strands show similar fault-zone widths, with mean values of  $59 \pm 17$  m ( $1\sigma$ ) and  $69 \pm 23$  m ( $1\sigma$ ),  
371 respectively (Figure S6).

372

373 The 2D strain maps show that the dilatational component of strain is largest at changes in the  
374 geometry of the rupture (Figure 4b), where for example, extensional strain (positive dilatation) is  
375 largest at sites of right transtensional fault bends. Along curvilinear segments, where there are  
376 subtle changes in the fault orientation, the sign of dilatation varies from negative (contraction) to  
377 positive (extensional) over short  $\sim 100$  m distances that correspond to subtle restraining and  
378 releasing bends of the fault (bottom right of Figure 4b along segment i). To understand how the  
379 width of the fault zone may vary according to the type of strain the fault experiences, we compare  
380 the fault zone width measurements along the mainshock rupture from within the transtensional  
381 bend (segment ii in Figure 4a) to a linear segment adjacent to it that experienced predominantly  
382 shear (segment i). Comparison of the distributions of the fault zone widths between these two  
383 neighboring segments shows a clear statistical difference (Figure S6). A one-tailed t-test shows  
384 that we can reject at the 5% confidence level that the two distributions of fault zone width have  
385 the same mean value between these two fault segments, indicating there are significantly wider  
386 fault zones within the transtensional bend (segment ii) undergoing tension than along the linear  
387 segment (segment i) that experienced mostly shear strain.

388

389 To understand a possible dependency of the fault zone width with the magnitude of contraction  
390 and extension the fault zone experiences we regress the measured fault zone widths from two km-  
391 scale right bends, a linear segment between these bends (Figure 4a) and two short transpressional

392 bends (see green boxes in Figure 1b for locations) with the magnitude of dilatation. Here we find  
393 wider fault zones along the transpressional and transtensional segments and narrowing in regions  
394 of decreasing dilatational strain (Figure 5a). To describe this dependency, we use a segmented  
395 regression analysis, which is a model choice supported by an F-test that shows a piecewise linear  
396 function provides a better fit over a linear one even when considering the effect of additional model  
397 parameters. Unfortunately, as there are simply not enough transpressional segments or restraining  
398 bends along the rupture we are unable to better populate the negative dilatation quadrant in our  
399 regression analysis (left side of Figure 5a). In addition, as illustrated by the wide 95% confidence  
400 interval bands we do not have sufficient constraint to test with confidence whether fault zones are  
401 wider under extension than contraction. Another limitation of the analysis is that due to the sparsity  
402 of field measurements along the transtensional segment (segment ii in Figure 4b) there are an  
403 insufficient number of OFD points (shown in Figures S3 and S4) to assess how the magnitude of  
404 distributed inelastic shear strain may scale with the degree of fault zone dilatation.

405

406 We also find a difference of the spatial distribution of deformation across the fault zone between  
407 the types of different fault geometries. This can be seen when comparing strain profiles across the  
408 transtensional bend (segment ii, Figure 4b) to the adjacent more linear rupture segment to the south  
409 (segment i). These profiles show a clear difference in how the inelastic dilatational and shear  
410 components of strain decay with distance away from the primary rupture between these two  
411 segments (Figure 5c). This suggests that not only can the differences in width of fault zones be  
412 resolved (a scalar quantity) but also the spatial distribution of inelastic strain across segments of  
413 different geometries.

414

415 The effect of the foreshock rupture on the distribution of strain across and along the mainshock  
416 rupture can also be clearly observed at the site where they intersect using the displacement,  
417 vorticity and dilatational strain maps (Figure 3). The dilatational strain field shows that the  
418 mainshock rupture experienced extension on the segment northwest of the intersection and  
419 contraction southeast of the intersection (Figure 3d), which is consistent with the expected location  
420 of unclamping and clamping, respectively, due to static stress changes imposed by slip along the  
421 foreshock rupture (e.g., Barnhart et al., 2019; Wang et al., 2020; Chen et al., 2020). In addition,  
422 we find a noticeable increase of the vorticity along the mainshock rupture that experienced positive

423 dilatation (unclamping) and a decrease relative to the segment that experienced negative dilatation  
424 (clamping) (which are labelled i) and ii) in Figure 3c). These differences in the amount of rotation  
425 between the two segments suggests a possible increase in the intensity of simple shear strain but  
426 this is not definitive evidence as the vorticity only captures the rotational component of simple  
427 shear. Therefore, to verify this we found from displacement profiles across the mainshock rupture  
428 that there is indeed a 20 cm increase of the total fault-parallel displacement from the clamped to  
429 the unclamped segment (Figure 3f). Profiles that measure the fault-perpendicular surface motion  
430 (Figure 3g) also clearly show the two fault mainshock rupture segments either side of the  
431 intersection experienced clamping (with a total of 50 cm of differential surface motion converging  
432 across the fault) and unclamping (a total of 40 cm of differential surface motion diverging away  
433 from the fault).

434

### 435 **3.2 Bookshelf kinematics**

436

437 Near the northern termination of the mainshock rupture the vorticity map shows a series of faults  
438 that are orthogonal to the main trend of the mainshock rupture that produce a symmetrical  
439 ‘hourglass’ shape (Figure 6). The vorticity maps reveal a series of parallel, NE-trending sinistral  
440 shear zones (red regions), that are bracketed to the southeast and northwest by conjugate and  
441 almost orthogonally orientated NW-trending dextral faults (blue regions). Between the series of  
442 parallel sinistral faults are zones of relatively large negative vorticity (blue regions in Figure 6a,  
443 also see 7a, b). We note that the vorticity cannot differentiate between rotations and distributed  
444 fracturing, but due to the pervasive distribution of these high vorticity values and the lack of  
445 observed distributed fracturing from field surveying (depicted as black lines in Figures 6a and 7a),  
446 the regions between the main faults are likely indicative of block rotations of up to  $\sim 0.12^\circ$ . These  
447 types of kinematics are indicative of bookshelf faulting, where the conjugate faults and intra-fault  
448 block rotations act to collectively accommodate regional dextral shear (McKenzie and Jackson,  
449 1983; Wesnousky, 2005). The different mechanisms by which the regional dextral shear is released  
450 can be seen first in the center of Figure 6a, where the total right-lateral shear is accommodated by  
451 a single dextral fault strand with a total offset  $\sim 1.6$  m, this offset is then partitioned further south  
452 between three parallel dextral fault strands, and then partitioned again further south amongst the  
453 conjugate sinistral faults and clockwise rotating blocks (Figure 6a and 7a, b).

454 To determine whether the observed kinematics of the co-seismic ruptures are consistent  
 455 with the longer-term pattern of cumulative shear and rotation expected by bookshelf kinematics  
 456 which has been found to describe the longer-term pattern of faulting elsewhere in nearby regions  
 457 (e.g., McKenzie and Jackson, 1983; Ron et al., 1984; Wesnousky, 2005), we compare the surface  
 458 motions measured in our displacement and vorticity maps to the kinematic relations of a bookshelf  
 459 fault system (McKenzie and Jackson, 1983; Platt and Becker, 2013). If the regional right-lateral  
 460 shear displacement ( $\gamma$ ) and the angle between the conjugate and bounding faults ( $\alpha$ ) are known,  
 461 then the amount of sinistral slip along the array of conjugate faults ( $\gamma'$ ) expected from bookshelf  
 462 faulting can be estimated from the following geometric relation (also see inset of Figure 6c).

463

$$464 \quad \gamma' = \gamma \cdot \cos(2\alpha) \quad (10)$$

465

466 The rotation of the blocks ( $\omega$ ) can be estimated from eq. 11 and assuming horizontal plane strain,  
 467 a component of contractional or extensional strain normal to the fault blocks ( $e$ ) can be estimated  
 468 from eq. 12, where  $l_b$  is the block length.

469

$$470 \quad \omega = \frac{\gamma}{2} \cdot (1 - \cos [2\alpha]) \quad (11)$$

471

$$472 \quad e = -\frac{\gamma}{2l_b} \cdot \sin (2\alpha) \quad (12)$$

473

474 From these relations and measuring  $\gamma = 1.6$  m and  $\alpha = 66^\circ$  (from Figure 6a) this predicts  $\gamma' = 1.0$   
 475 m,  $e=0.044\%$  strain and  $\omega = 0.05^\circ$  (see Table 2). These predicted values compare well with those  
 476 observed from the strain and displacement maps (Figure 6a and 7), where we find  $\gamma' = 0.8$  m  
 477 (measured from the southernmost sinistral fault),  $e=0.04\%$  strain (measured from within the  
 478 bookshelf blocks, see Figure S7) and  $\omega = 0.06^\circ$  (mean value estimated from within the  
 479 southernmost ‘block’ in Figure 6), which show the observed kinematics are consistent with  
 480 bookshelf faulting.

481

482 To test whether the foreshock and mainshock cross-faulting are a larger-scale version of the same  
 483 bookshelf tectonics shown in Figure 6a and c, we again use the kinematic bookshelf relations to



484 compare its predictions against the observed displacements at the macroscopic scale (McKenzie  
 485 and Jackson, 1983; Platt and Becker, 2013). From measuring the mean slip along the mainshock  
 486 strand immediately adjacent to the foreshock strand we find  $\gamma = 0.98$  m and the angle between the  
 487 mainshock-foreshock strands is  $\alpha = 86^\circ$ . From this we find the predicted slip on the foreshock fault  
 488 is  $\gamma' = 0.97$  m which falls within the variation of observed values (mean observed sinistral  
 489 displacement of  $0.71 \pm 0.33$  m,  $1\sigma$ , and maximum of 1.40 m, Figure 2).

490  
 491 We can also estimate the total amount of long-term cumulative displacement ( $d_{fore}$ ) accrued along  
 492 the conjugate sinistral foreshock fault (the strand west of the mainshock strand) since its initiation.  
 493 To do this we use a simple geometric expression that relates  $d_{fore}$  to the amount of total block  
 494 rotation that has occurred across a zone of simple shear (Freund, 1974; Ron et al., 1984). Assuming  
 495 only plane strain,  $d_{fore}$  is related to: the width of fault-bounded blocks ( $w_b$ , see Figure 6c), the initial  
 496 angle between the conjugate faults when they first formed ( $\alpha_i$ ) and the total amount of rotation  
 497 since they formed ( $\omega_T$ ) as defined by the following relation (Freund, 1974; Ron et al., 1984),

$$499 \quad d_{fore} = w_b \left[ \frac{\sin(\omega_T)}{\sin(\alpha) \cdot \sin(\alpha - \omega_T)} \right] \quad (13)$$

500  
 501 The width of the block ( $w_b = 4.89$  km) is measured as the distance between the foreshock fault  
 502 west of the mainshock strand to another parallel SW-trending fault to the south (see Figure 6c).  
 503 This gives an aspect ratio of the crustal block (width/length) of 0.37 which is consistent with the  
 504 aspect ratios of the smaller blocks in Figure 6a, that have a mean value of 0.35 ( $n = 5$ ). The total  
 505 amount of rotation of the foreshock fault ( $\omega_T = 3-7^\circ$ ) is estimated from the difference of its average  
 506 azimuth (N43°E) with the azimuth of the smaller conjugate sinistral faults shown in Figure 6a  
 507 (with minimum and maximum values ranging from N36-40°E). This assumes that the much shorter  
 508 sinistral faults (ranging in lengths from 200 – 1300 m) shown in Figure 6a are close to their initial  
 509 orientation when they developed. The initial angle between the conjugate foreshock faults and the  
 510 bounding dextral mainshock faults is assumed as  $\alpha = 90^\circ$  (a value also used for conjugate faults  
 511 further north in the Walker Lane [see Wesnousky, 2005]). This gives  $d_{fore} = 256-600$  m, which  
 512 indicates that the foreshock fault is highly structurally immature.

513

514 **4. Discussion**

515

516 **4.1. Effect of Off-fault Deformation on Rupture**

517

518 Experimental and theoretical studies show that the rupture propagation through the near-surface  
519 (< 5 km depth) can be inhibited by a range of mechanisms, including velocity-strengthening  
520 frictional properties of the sliding fault in the near-surface, generation of plastic strain during  
521 rupture, and frictional sliding on pre-existing fractures that can dissipate the rupture energy (Fialko  
522 et al., 2005; Sammis et al., 2010; Kaneko and Fialko, 2011; Gabriel et al., 2013). These  
523 mechanisms may explain why some earthquakes exhibit significantly lower slip at the surface than  
524 at seismogenic depths (6-10 km), which has been termed the shallow slip deficit (Fialko et al.,  
525 2005), and why ruptures with faster velocities are observed along more mature structurally  
526 developed smoother faults, e.g., the 1999  $M_w$  7.4 Izmit, 2001  $M_w$  7.8 Kokoxili, 2002  $M_w$  7.9 Denali  
527 and 2018  $M_w$  7.5 Palu earthquakes (Bouchon et al., 2001, 2010; Ozacar and Beck, 2004; Bao et  
528 al., 2019; Socquet et al., 2019).

529

530 As faults accumulate displacement over geologic timescales, they are thought to evolve or ‘mature’  
531 progressively from a network of disorganized and disconnected segments that are separated by  
532 geometrical complexities (such as stepovers, bends and branches), to a structurally simplified  
533 system or sometimes single throughgoing fault (Tchalenko, 1970; Wesnousky, 1988; Stirling et  
534 al., 1996). This structural evolution can occur via a range of fault growth and strain weakening  
535 feedback processes (Ben-Zion & Sammis, 2003; Faulkner & Mitchell, 2011). A consequence of  
536 this evolutionary process is that as strain progressively localizes to the fault core, distributed  
537 fractures become abandoned (Frost et al., 2009). This is manifest by a decreasing density of  
538 stepovers at the macroscopic scale (Wesnousky, 1988) and decreasing amounts of distributed off-  
539 fault inelastic strain (Dolan and Haravitch, 2014). Here we find OFD for the foreshock is much  
540 larger than the mainshock (56% and 34% respectively), which we interpret as indicating the faults  
541 involved in the foreshock rupture have a lower degree of strain localization and are therefore less  
542 structurally developed (Dolan and Haravitch, 2014). To support this inference, we have assessed  
543 a number of other relevant factors, which includes both qualitatively and quantitatively comparing  
544 the geometrical fault complexity of the foreshock to the mainshock. First, surface rupture mapping

545 from daily Planet Labs imagery, which can uniquely separate the two events in time (Milliner &  
546 Donnellan, 2020), show the foreshock is clearly more structurally complex with a higher number  
547 of disorganized segments (see Figure S8). Second, from estimating the density of major stepovers  
548 (with > 1 km width, following the approach of Wesnousky [1988]) we find it is almost a factor of  
549 two higher for the foreshock (0.157 stepovers/unit length) than the mainshock (0.08), again  
550 showing the foreshock involved a more disconnected fault system. Lastly, measurements of offset  
551 Late Jurassic dikes across the southern end of the Ridgecrest mainshock rupture found a  
552 cumulative displacement of 1.6 km, although there are no available geomorphic features to  
553 estimate a value across the foreshock rupture (Andrew & Walker, 2020). However, this value of  
554 1.6 km is much larger than our estimated cumulative displacement for the faults involved in the  
555 foreshock rupture of 256-600 m, suggesting a clear difference in the structural maturity. Although  
556 there is not a known independent estimate of the cumulative displacement for the foreshock rupture  
557 to verify possible differences in the relative structural maturity of the faults involved in the two  
558 ruptures, our results do show clear differences in the degree of strain localization, structural  
559 organization and significant differences in estimates of the cumulative displacement assuming  
560 bookshelf type kinematics.

561  
562 Here, we assess whether faults that have larger OFD (i.e., larger amounts of distributed inelastic  
563 strain and are therefore likely less mature), have slower rupture velocities and more pronounced  
564 shallow slip deficits. The mean OFD measured along the mainshock rupture ( $34 \pm 10\%$ ) is similar  
565 in magnitude to that measured along other nearby surface ruptures including the 1992  $M_w$  7.3  
566 Landers and 1999  $M_w$  7.1 Hector Mine events (which had OFD of  $46 \pm 10\%$  and  $39 \pm 22\%$ ,  
567 respectively, which we note were estimated using the same field-optical displacement comparison  
568 approach [Milliner et al., 2016]), and are fault systems that are known to be immature (with 3-4  
569 km of cumulative displacement [Jachens et al. 2002]). Interestingly, all three of these relatively  
570 immature NW-trending dextral fault systems exhibit relatively similar slow rupture velocities of  
571  $\sim 2.7$  km/s, 2.2 km/s, and 2 km/s for the Landers, Hector Mine and Ridgecrest events, respectively  
572 (Chen et al., 2020; Goldberg et al., 2020; Ji et al., 2002; Liu et al., 2019; Peyrat et al., 2001; Ross  
573 et al., 2019), consistent with the notion that slower ruptures occur along faults of higher OFD with  
574 more complex multi-segment rupture geometries.

575

576 The larger amount of OFD found for the foreshock (56%) than the mainshock rupture (34%),  
577 provides another and more direct means to compare the possible effect of off-fault distributed  
578 strain on the shallow slip deficit and rupture velocity. Current seismic inversion models of the  
579 rupture do not show a significant difference of the velocity between the two events, finding they  
580 are both  $\sim 2$  km/s (Chen et al., 2020; Goldberg et al., 2020; Ross et al., 2019; Wang et al., 2020).  
581 However, the lack of a resolvable difference could result from limitations of the inversion method  
582 such as the model resolution, data constraints and sensitivity, or inherent trade-offs (e.g., see Figure  
583 S4 of Chen et al., 2020 for the range of possible velocities). An additional complication is that it  
584 is possible the mainshock rupture velocity could have been inhibited by a decrease of static  
585 Coulomb stress applied by the foreshock rupture, as high shear pre-stresses along faults are thought  
586 to cause faster rupture velocities (Bao et al., 2019). However, this effect of reduced pre- shear  
587 stress is likely to be small in this case, given slip inversion models estimate a minor change ( $\sim 0.2$   
588 MPa) compared to the total stress drop (10 MPa), (Barnhart et al., 2019; Chen et al., 2020).  
589 Therefore, it is not immediately clear if the rupture velocities between the foreshock and  
590 mainshock are significantly similar or not, or the effect of local pre-stress changes, which  
591 complicates understanding the effect of OFD on the efficiency of rupture propagation.

592  
593 To assess differences in the variation of slip with depth between the  $M_w$  6.4 foreshock and  $M_w$  7.1  
594 mainshock events we compiled slip distributions from four available geodetic and seismic slip  
595 inversion studies (Chen et al., 2020; Jin and Fialko, 2019; Xu et al., 2020; Wang et al., 2020).  
596 Although there is a wide variation of the slip-depth distributions between the various slip inversion  
597 models, which reflects the epistemic uncertainty due to varying model parameterizations, inversion  
598 strategies and data types, there are still systematic differences between the foreshock and  
599 mainshock events (Figure 8). Estimating the shallow slip deficit as the percent difference of surface  
600 slip to the maximum at depth, we find a more pronounced shallow slip deficit for the foreshock  
601 (ranging from 42-65%) than the mainshock (18-35%), consistent with the notion that more  
602 immature faults that exhibit larger amounts of inelastic strain (i.e., OFD) correspond to larger  
603 shallow slip deficits (as proposed by Kaneko & Fialko, 2011). In contrast, the shallow slip deficit  
604 estimates of the 1992 Landers and 1999 Hector Mine events from geodetic inversions show much  
605 smaller values at 18% and 3%, respectively (Xu et al., 2016). The apparent similar amounts of  
606 inelastic strain (34%, 46% and 39% OFD) but differing shallow slip deficits (18-35%, 18%, and

607 3%) between these three large events (Ridgecrest, Landers and Hector Mine, respectively)  
608 conflicts with the expectation that the former may influence the latter. This may suggest the  
609 importance of other processes in affecting the efficiency of rupture propagation through the near-  
610 surface such as sediment thickness and type, pre-stress on the fault, frictional properties, or  
611 dilatancy strengthening (Rice, 1975; Marone et al., 1991; Kaneko and Fialko, 2011; Dolan and  
612 Haravitch, 2014).

613

#### 614 **4.2. Inelastic strain and the effect of fault zone dilatation**

615

616 From comparison of the measured fault zone width with the dilatational component of the 2D  
617 strain tensor we find that both the scalar width and decay rate of inelastic strain away from the  
618 main rupture are wider and slower in regions of extension and contraction than shear (Figure 5).  
619 We find that the magnitude and sense of dilatational strain (i.e., contraction or extension), varies  
620 according to the fault geometry and orientation, with extensional strain expectedly largest along  
621 releasing fault bends (Figures 3 and 4). This is consistent with previous work that have found  
622 correlations of the scalar fault width or OFD with the fault geometry along oblique-normal strike-  
623 slip faults (Scott et al., 2018; Teran et al., 2015). Along the Ridgecrest rupture we have shown that  
624 these geometries alter the type of strain the fault zone experiences and that such strain is partitioned  
625 differently between the shear and dilatational components (Figure 4a and b).

626

627 Constraining how fast or slow inelastic strain decays away from the primary rupture holds  
628 importance for better characterizing the hazard of distributed fault rupture, which is needed to  
629 effectively engineer structures to withstand its effect (e.g., for roads, pipelines or bridges that  
630 cannot avoid fault crossings). As more confidence is known of what parameters control the spatial  
631 distribution of inelastic strain across a surface rupture (e.g., the type of fault geometry or sediment  
632 thickness) through increasing observational constraint, this will help explain more of the total  
633 variance of the fault zone width along the lengths of ruptures. In doing so this will reduce the  
634 epistemic uncertainty of empirically constrained probabilistic fault displacement hazard models  
635 and improve their predictive power (e.g., Petersen et al., 2011). For example, our results show that  
636 transtensional bends have a different level of distributed rupture hazard, with a higher probability  
637 of experiencing distributed rupture further away from the primary fault, than segments that

638 experience predominantly shear strain (Figure 5b and c). This would therefore justify developing  
639 separate fault displacement prediction equations for differing fault geometries into probabilistic  
640 fault displacement hazard analysis.

641

### 642 **4.3 Orthogonal faulting due to Bookshelf kinematics**

643

644 Bookshelf faulting is thought to initiate from simple shear being accommodated by conjugate pairs  
645 of synthetic (R) and antithetic (R') Riedel shears across a trans-tensional step-over region  
646 (Wesnousky, 2005). Over time, as the Riedel fractures accumulate slip, the primary *en-echelon* R  
647 shears coalesce to form a single through-going fault strand, while the R' shears located within the  
648 stepover are progressively rotated and become increasingly more oblique to the R shears,  
649 eventually forming a set of orthogonal faults. Here, we find that the observed displacements along  
650 the orthogonal set of faults involved in the foreshock and mainshock ruptures are consistent with  
651 the kinematics expected by bookshelf faulting indicating they are a larger scale, more-developed  
652 system of the bookshelf faulting observed at the smaller scale in Fig 6a and c. In addition, the  
653 asymmetric triangular distribution of slip along the foreshock rupture (at the ~10 km scale) bears  
654 a strong similarity to that of slip along the smaller sinistral conjugate faults shown in Figure 6d (at  
655 the ~100 m scale, also see Figure S9 for comparison). Such bookshelf faulting which involves  
656 progressive rotation of conjugate faults to orientations that become highly oblique could also  
657 explain the wide-spread distribution of orthogonal aftershocks at other length scales in this region  
658 (Ross et al., 2019). A bookshelf system at the ~10 km scale also suggests that the Little Lake and  
659 Airport Fault Zones (LLFZ and APFZ) would form the western-most bounding NW-trending  
660 dextral fault. This provides a possible explanation as to why the foreshock rupture terminated  
661 surprisingly at a site of peak slip in the southwest (~1.4 m, Figure 2), simply because it is  
662 structurally controlled by the bookshelf kinematics; i.e., west of the LLFZ and APFZ there is likely  
663 little-no rotations of crustal blocks which means sinistral slip is not kinematically required and  
664 therefore the foreshock fault simply does not extend further west.

665

666 However, one notable difference from the bookshelf initiation framework proposed by Wesnousky  
667 (2005) is that the bookshelf faulting found specifically at the northern end of the mainshock rupture  
668 (Figures 6 and 7) does not seem to occur within a transtensional step. Here there are clearly no

669 dextral faults that extend to either side to ‘bound’ the sinistral faults that would satisfy the  
670 definition of a stepover, nor does the rupture step to the right that would produce transtension and  
671 the dilatation map shows no evidence of significant extension. Instead, the clockwise rotation and  
672 sinistral faulting found here are located directly beyond the tips of and between three north-west  
673 trending dextral faults (one to the north and the other two to the south), producing an ‘hourglass’  
674 geometry. We argue another possible mechanism in which bookshelf kinematics could arise is due  
675 to the transition of shear strain to rotation beyond fault tips (like that shown by the vorticity map,  
676 Figure 6a). In the case here, two or more faults do not align or connect, which creates a zone of  
677 distributed clockwise rotation. For the dextral shear to be accommodated over a region (in this  
678 case this is ~2 m of dextral motion distributed over an ~1.5 km wide zone across the ‘bookshelf’,  
679 see Figure 7d) it can be shown that both clockwise rotation (illustrated in Figure 6a and 7d) and  
680 perpendicular sinistral shear is required (shown in Figure 7c, where such strain is responsible for  
681 producing the series of parallel sinistral fractures), as the summation of the displacement gradients  
682 of both these types of surface motion are equivalent to dextral shear and does not require  
683 transtensional strain (Platt, 2017). A similar behavior of bookshelf faulting was also observed from  
684 relocated aftershocks of the 1986  $M_L$  5.7 Mount Lewis earthquake, CA (Kilb et al. 2002). The  
685 seismicity showed a series of orthogonal sinistral faults that were not located within a stepover but  
686 instead directly beyond the tips of a dextral fault, which produced a similar ‘hourglass’ shaped  
687 feature as observed here (also see Kim et al., 2004). For the kinematics found specifically at the  
688 northern end of the Ridgecrest rupture, the cause of bookshelf faulting seems to be more consistent  
689 with how shear strain transitions beyond fault tips to rotation (i.e., a type of fault termination  
690 structure) than a result of distributed transtensional shear across a right-stepover which is a  
691 mechanism more applicable to faulting within the Mina deflection further north in the Walker Lane  
692 (Wesnousky, 2005).

693

694 We note that although the progressive rotation of faults over geologic timescales due to bookshelf  
695 kinematics is one possible explanation for the occurrence of orthogonal faults into an unfavorable  
696 orientation relative to the background stress state, lab and theoretical studies have shown that  
697 during rupture the dynamic stresses locally along faults can rotate away from the far-field stresses  
698 which can cause failure of faults with orthogonal geometries (Rousseau and Rosakis, 2003; Xu &  
699 Ben-Zion, 2013). Therefore, it is possible that both progressive rotation of faults over geologic

700 timescales due to bookshelf kinematics and rotation of stresses locally along faults during rupture  
701 could explain the generation and slip of orthogonal faults that are seemingly unfavorable with  
702 respect to the regional, far-field, background stress state.

703  
704 A number of major northwest trending dextral faults in the ECSZ seem to stop abruptly at major  
705 orthogonally orientated sinistral faults (such as the Garlock or Pinto Mountain faults, see Figure  
706 6e). The lack of a physical connection makes it unclear how the regional right-lateral shear strain  
707 is accommodated across these fault gaps and how these junctions evolve over geologic timescales.  
708 A lack of paleomagnetic data specifically at these fault gaps also make it difficult to understand  
709 the role of crustal rotations in accommodating this long-term regional dextral strain. Here the  
710 vorticity map shows clear regions of relatively large clockwise rotation adjacent to NE-trending  
711 sinistral faults (Figure 6a). Observations from field mapping of the rupture do not show pervasive  
712 fracturing in these regions, which confirms that much of the large negative vorticity values most  
713 likely reflect crustal rotations (that range up to  $\sim 0.1^\circ$ ). The vorticity map also shows that neither  
714 the northern nor the southern set of conjugate sinistral faults (i.e., within either end of the  
715 ‘hourglass’ feature) intersect or displace the NW-trending dextral faults but are instead embedded  
716 within regions of clockwise rotation. This provides one possible explanation as to why NW-  
717 trending dextral faults do not physically connect with neighboring NE-trending sinistral faults,  
718 simply because dextral brittle shear strain transitions beyond their tips to zones of clockwise  
719 rotation as previously hypothesized (Andrew and Walker, 2017). As mentioned, dextral shear is  
720 kinematically equivalent to the sum of surface motion from orthogonally orientated sinistral shear  
721 and clockwise rotation (Platt, 2017). Therefore, our observations of coseismic strain release we  
722 believe are analogous and support the kinematic argument that the remaining component of long-  
723 term dextral strain across regions of fault gaps is likely accommodated by clockwise rotation that  
724 explains the lack of a physical fault connection or continuation of local dextral strain (i.e., that  
725 shown in Figure 6a).

726

## 727 **Conclusions**

728

729 Measurements of surface motion across the Ridgecrest surface rupture from high-resolution optical  
730 image correlation provide empirical constraints of the effect of contraction and extension on the



731 width of the fault zone. The results show that as expected, faults are clearly wider under extension  
732 and contraction than lateral shear, but we are unable to discern whether they are wider under  
733 extension than contraction. This relation also helps explain the apparent correlation of fault  
734 geometrical complexities with wider faults zones, as variations of the fault orientation alter the  
735 local stress state, causing fault-perpendicular strain that is not equally partitioned across the fault  
736 zone between the dilatational and shear strain components. Observations of how the inelastic strain  
737 attenuates with distance from the primary rupture (Figure. 4 b, c) also suggests there are different  
738 hazard probabilities of distributed rupture for transpressional and transtensional bends compared  
739 to simpler, more linear segments of the rupture that experience predominantly shear strain. We  
740 suggest these differences could be accounted for by developing separate fault displacement  
741 prediction equations for different fault geometries when incorporating them into probabilistic fault  
742 displacement hazard analysis (PFDHA).

743

744 Our analysis shows that the faults involved in both the foreshock and mainshock ruptures are both  
745 structurally immature and that the former is likely less structurally developed as we find a higher  
746 amount of distributed inelastic strain (with average off-fault deformation amounts of  $56 \pm 10\%$   
747 and  $34 \pm 10\%$ , respectively). The structural immaturity of the foreshock faults is also supported  
748 by an estimate of its cumulative displacement, which is found from approximating the kinematics  
749 to bookshelf motion, that gives a relatively low total amount of 250-600 m. The larger amount of  
750 off-fault deformation and inferred lower structural maturity for the foreshock faults shows a fault  
751 system with higher amounts of near-surface distributed inelastic strain and poorer fault linkage.  
752 These are all thought to affect the efficiency of rupture propagation through the shallow surface,  
753 which could explain why the foreshock rupture exhibits a higher slip deficit than the more mature  
754 and structurally simplified mainshock rupture (Wesnousky, 1988; Kaneko & Fialko, 2011; Dolan  
755 and Haravitch, 2014).

756

757 We propose that bookshelf faulting provides a concise and useful framework to explain a number  
758 of questions regarding the faulting kinematics of this region at the local and regional scale. Our  
759 measurements of 2D strain and rotation show, i) faults do not intersect one another because dextral  
760 strain transitions to clockwise rotation beyond their tips, ii) cross-faulting and aftershock  
761 distributions arise because of a history of progressive clockwise rotation over geologic time of

762 conjugate faults that accommodate simple shear, iii) the foreshock-mainshock ruptures are likely  
763 a larger scale version of ‘bookshelf faulting’ which can explain the southwestern termination point  
764 of the foreshock event because it structurally abuts the Little Lake fault zones that mark the west-  
765 bounding ‘bookshelf’ fault.

766

767

## 768 **Acknowledgements**

769

770 We would like to thank the reviewers Chelsea Scott, Mike Oskin and Shiqing Xu for their helpful  
771 suggestions, and Cecile Lasserre and Isabelle Manighetti for their comments that helped strengthen  
772 and clarify aspects of our study. We also thank Alex Morelan, Tim Dawson, Kate Scharer, for their  
773 helpful discussions and sharing of data as well as the many field geologists who cannot all be  
774 mentioned here who provided the invaluable and detailed field survey measurements of the surface  
775 ruptures. **Funding:** Part of this research was supported by the NASA Earth Surface and Interior  
776 focus area and performed at the Jet Propulsion Laboratory, California Institute of Technology  
777 (80NM0018D0004). Funding for this project was provided under a NASA Postdoctoral Program  
778 fellowship to C.M. administered by the Universities Space and Research Association through a  
779 contract with NASA. Satellite imagery for this project were purchased under SCEC grant #19222.

780 **Author contributions:** All authors contributed to this study and participated in manuscript  
781 revision. Competing interests: The authors declare that they have no competing interests. **Data**  
782 **and materials availability:** Please see supplementary datasets or the Zenodo open repository  
783 (<http://doi.org/10.5281/zenodo.3937853>) containing measurements of the coseismic fault slip,  
784 fault zone width and off-fault deformation

785

786

787

## 788 **References**

789

790 Allam A.A., Kroll K.A., Milliner C.W., Richards-Dinger K.B. Effects of fault roughness on  
791 coseismic slip and earthquake locations. *Journal of Geophysical Research: Solid Earth*.  
792 2019 Nov;124(11):11336-49

793 Amos, C.B., Brownlee, S.J., Rood, D.H., Fisher, G.B., Bürgmann, R., Renne, P.R. and Jayko,  
794 A.S., 2013. Chronology of tectonic, geomorphic, and volcanic interactions and the tempo  
795 of fault slip near Little Lake, California. *Bulletin*, 125(7-8), pp.1187-1202.

796 Anderson, E.M., 1951. The dynamics of faulting and dyke formation with applications to Britain.  
797 Oliver and Boyd, Edinburgh.

798 Andrew, J.E., Walker, J.D. and Monastero, F.C., 2015. Evolution of the central Garlock fault  
799 zone, California: A major sinistral fault embedded in a dextral plate  
800 margin. *Bulletin*, 127(1-2), pp.227-249.

801 Andrew, J.E., Walker, J.D., 2017. Path and amount of dextral fault slip in the Eastern California  
802 shear zone across the central Mojave Desert. *GSA Bull.* 129, 855–868.  
803 <https://doi.org/10.1130/B31527.1>

804 Andrew J.E., Walker, J.D., 2020, Total Slip Estimates of the M7.1 (July 2019) Seismogenic  
805 Airport Lake Fault System, Ridgecrest, California, GSA meeting. Abstract: 31-4

806 Bao, H., Ampuero, J.-P., Meng, L., Fielding, E.J., Liang, C., Milliner, C.W.D., Feng, T., Huang,  
807 H., 2019. Early and persistent supershear rupture of the 2018 magnitude 7.5 Palu  
808 earthquake. *Nat. Geosci.* 12, 200–205. <https://doi.org/10.1038/s41561-018-0297-z>

809 Barnhart, W.D., Hayes, G.P., Gold, R.D., 2019. The July 2019 Ridgecrest, California,  
810 Earthquake Sequence: Kinematics of Slip and Stressing in Cross-Fault Ruptures.  
811 *Geophys. Res. Lett.* 46, 11859–11867. <https://doi.org/10.1029/2019GL084741>

812 Becker, T.W., Hardebeck, J.L., Anderson, G., 2005. Constraints on fault slip rates of the  
813 southern California plate boundary from GPS velocity and stress inversions. *Geophys. J.*  
814 *Int.* 160, 634–650. <https://doi.org/10.1111/j.1365-246X.2004.02528.x>

815 Ben-Zion Y, Sammis CG. Characterization of fault zones. *Pure and applied geophysics.* 2003  
816 Mar 1;160(3-4):677-715.

817 Bouchon, M., Bouin, M.-P., Karabulut, H., Toksöz, M.N., Dietrich, M., Rosakis, A.J., 2001.  
818 How fast is rupture during an earthquake? New insights from the 1999 Turkey  
819 Earthquakes. *Geophys. Res. Lett.* 28, 2723–2726. <https://doi.org/10.1029/2001GL013112>

820 Bouchon, M., Karabulut, H., Bouin, M.-P., Schmittbuhl, J., Vallée, M., Archuleta, R., Das, S.,  
821 Renard, F., Marsan, D., 2010. Faulting characteristics of supershear earthquakes.  
822 *Tectonophysics* 493, 244–253. <https://doi.org/10.1016/j.tecto.2010.06.011>

823 Brandenberg, S.J., Stewart, J.P., Wang, P., Nweke, C.C., Hudson, K., Goulet, C.A., Meng, X.,  
824 Davis, C.A., Ahdi, S.K., Hudson, M.B., Donnellan, A., Lyzenga, G., Pierce, M., Wang,  
825 J., Winters, M.A., Delisle, M.-P., Lucey, J., Kim, Y., Gallien, T.W., Lyda, A., Yeung,  
826 J.S., Issa, O., Buckreis, T., Yi, Z., 2020. Ground Deformation Data from GEER  
827 Investigations of Ridgecrest Earthquake Sequence. *Seismol. Res. Lett.*  
828 <https://doi.org/10.1785/0220190291>

829 Brooks, B.A., Minson, S.E., Glennie, C.L., Nevitt, J.M., Dawson, T., Rubin, R., Ericksen, T.L.,  
830 Lockner, D., Hudnut, K., Langenheim, V., Lutz, A., Mareschal, M., Murray, J., Schwartz,  
831 D., Zaccane, D., 2017. Buried shallow fault slip from the South Napa earthquake  
832 revealed by near-field geodesy. *Sci. Adv.* 3, e1700525.  
833 <https://doi.org/10.1126/sciadv.1700525>

834 Bruhat L, Klinger Y, Vallage A, Dunham EM. Influence of fault roughness on surface  
835 displacement: from numerical simulations to coseismic slip distributions. *Geophysical*  
836 *Journal International*. 2020 Mar;220(3):1857-77.

837 Chen, K., Avouac, J.-P., Aati, S., Milliner, C., Zheng, F., Shi, C., 2020. Cascading and pulse-like  
838 ruptures during the 2019 Ridgecrest earthquakes in the Eastern California Shear Zone.  
839 *Nat. Commun.* 11, 22. <https://doi.org/10.1038/s41467-019-13750-w>

840 Dawson, T.E., McGill, S.F. and Rockwell, T.K., 2003. Irregular recurrence of paleoearthquakes  
841 along the central Garlock fault near El Paso Peaks, California. *Journal of Geophysical*  
842 *Research: Solid Earth*, 108(B7). [doi.org/10.1029/2001JB001744](https://doi.org/10.1029/2001JB001744)

843 Dolan, J.F. and Haravitch, B.D., 2014. How well do surface slip measurements track slip at  
844 depth in large strike-slip earthquakes? The importance of fault structural maturity in  
845 controlling on-fault slip versus off-fault surface deformation. *Earth and Planetary*  
846 *Science Letters*, 388, pp.38-47.

847 Dolan, J.F., McAuliffe, L.J., Rhodes, E.J., McGill, S.F., Zinke, R., 2016. Extreme multi-  
848 millennial slip rate variations on the Garlock fault, California: Strain super-cycles,  
849 potentially time-variable fault strength, and implications for system-level earthquake  
850 occurrence. *Earth Planet. Sci. Lett.* 446, 123–136.  
851 <https://doi.org/10.1016/j.epsl.2016.04.011>

852 Dor O, Ben-Zion Y, Rockwell TK, Brune J. Pulverized rocks in the Mojave section of the San  
853 Andreas Fault Zone. (2006) *Earth and Planetary Science Letters*. May 30;245(3-4):642-54.

854 DuRoss, C. B., R. D. Gold, T. E. Dawson, K. M. Scharer, K. J. Kendrick, S. O. Akciz, S. J. Angster,  
855 J. Bachhuber, S. Bacon, S. EK. Bennett, et al. (2020). Surface Displacement Distributions  
856 for the July 2019 Ridgecrest, California, Earthquake Ruptures, *Bull. Seismol. Soc. Am.*  
857 *XX*, 1–19, doi: 10.1785/0120200058

858 Dunham, E.M., Belanger, D., Cong, L., Kozdon, J.E., 2011. Earthquake Ruptures with Strongly  
859 Rate-Weakening Friction and Off-Fault Plasticity, Part 1: Planar Faults Earthquake  
860 Ruptures with Strongly Rate-Weakening Friction and Off-Fault Plasticity, Part 1: Planar  
861 Faults. *Bull. Seismol. Soc. Am.* 101, 2296–2307. <https://doi.org/10.1785/0120100075>

862 Dziewonski, A. M., T.-A. Chou and J. H. Woodhouse, 1981, Determination of earthquake source  
863 parameters from waveform data for studies of global and regional seismicity, *J. Geophys.*  
864 *Res.*, 86, 2825-2852, 1981. doi:10.1029/JB086iB04p02825

865 Ekström, G., M. Nettles, and A. M. Dziewonski, 2012, The global CMT project 2004-2010:  
866 Centroid-moment tensors for 13,017 earthquakes, *Phys. Earth Planet. Inter.*, 200-201, 1-  
867 9,. doi:10.1016/j.pepi.2012.04.002

868 Faulkner DR, Mitchell TM, Jensen E, Cembrano J. Scaling of fault damage zones with  
869 displacement and the implications for fault growth processes. *Journal of Geophysical*  
870 *Research: Solid Earth.* 2011 May;116(B5).

871 Fialko, Y., Sandwell, D., Simons, M., Rosen, P., 2005. Three-dimensional deformation caused  
872 by the Bam, Iran, earthquake and the origin of shallow slip deficit. *Nature* 435, 295.  
873 <https://doi.org/10.1038/nature03425>

874 Frankel, K.L., Glazner, A.F., Kirby, E., Monastero, F.C., Strane, M.D., Oskin, M.E., Unruh, J.R.,  
875 Walker, J.D., Anandakrishnan, S., Bartley, J.M., Coleman, D.S., Dolan, J.F., Finkel,  
876 R.C., Greene, D., Kylander-Clark, A., Marrero, S., Owen, L.A., Phillips, F., 2008. Active  
877 tectonics of the eastern California shear zone, in: *GSA Field Guide 11: Field Guide to*  
878 *Plutons, Volcanoes, Faults, Reefs, Dinosaurs, and Possible Glaciation in Selected Areas*  
879 *of Arizona, California, and Nevada.* Geological Society of America, pp. 43–81.  
880 [https://doi.org/10.1130/2008.fld011\(03\)](https://doi.org/10.1130/2008.fld011(03))

881 Freund, R., 1974. Kinematics of transform and transcurrent faults. *Tectonophysics* 21, 93–134.  
882 [https://doi.org/10.1016/0040-1951\(74\)90064-X](https://doi.org/10.1016/0040-1951(74)90064-X)

883 Frost E, Dolan J, Sammis C, Hacker B, Cole J, Ratschbacher L. (2009) Progressive strain  
884 localization in a major strike-slip fault exhumed from midseismogenic depths: Structural

885 observations from the Salzach-Ennstal-Mariazell-Puchberg fault system, Austria. *Journal*  
886 *of Geophysical Research: Solid Earth*. Apr;114(B4).

887 Gabriel, A.-A., Ampuero, J.-P., Dalguer, L.A., Mai, P.M., 2013. Source properties of dynamic  
888 rupture pulses with off-fault plasticity. *J. Geophys. Res. Solid Earth* 118, 4117–4126.  
889 <https://doi.org/10.1002/jgrb.50213>

890 Ganev, P.N., Dolan, J.F., McGill, S.F., Frankel, K.L., 2012. Constancy of geologic slip rate  
891 along the central Garlock fault: implications for strain accumulation and release in  
892 southern California. *Geophys. J. Int.* 190, 745–760. [https://doi.org/10.1111/j.1365-](https://doi.org/10.1111/j.1365-246X.2012.05494.x)  
893 [246X.2012.05494.x](https://doi.org/10.1111/j.1365-246X.2012.05494.x)

894 Gold, R.D., Reitman, N.G., Briggs, R.W., Barnhart, W.D., Hayes, G.P., Wilson, E., 2015. On-  
895 and off-fault deformation associated with the September 2013 Mw 7.7 Balochistan  
896 earthquake: Implications for geologic slip rate measurements. *Tectonophysics* 660, 65–  
897 78. <https://doi.org/10.1016/j.tecto.2015.08.019>

898 Goldberg, D.E., Melgar, D., Sahakian, V.J., Thomas, A.M., Xu, X., Crowell, B.W., Geng, J.,  
899 2020. Complex Rupture of an Immature Fault Zone: A Simultaneous Kinematic Model of  
900 the 2019 Ridgecrest, CA Earthquakes. *Geophys. Res. Lett.* 47, e2019GL086382.  
901 <https://doi.org/10.1029/2019GL086382>

902 Hardebeck, J. L. (2020). A Stress-Similarity Triggering Model for Aftershocks of the Mw 6.4  
903 and 7.1 Ridgecrest Earthquakes, *Bull. Seismol. Soc. Am.* 110, 1716–1727, doi:  
904 [10.1785/0120200015](https://doi.org/10.1785/0120200015)

905 Hatem AE, Cooke ML, Toeneboehn K. Strain localization and evolving kinematic efficiency of  
906 initiating strike-slip faults within wet kaolin experiments. *Journal of Structural Geology*.  
907 2017 Aug 1;101:96-108.

908 Hauksson E. State of stress from focal mechanisms before and after the 1992 Landers earthquake  
909 sequence. *Bulletin of the Seismological Society of America*. 1994 Jun 1;84(3):917-34.

910 Herbert, J.W., Cooke, M.L., Oskin, M., Difo, O., 2014. How much can off-fault deformation  
911 contribute to the slip rate discrepancy within the eastern California shear zone? *Geology*  
912 42, 71–75. <https://doi.org/10.1130/G34738.1>

913 Hudnut, K.W., Seeber, L., Pacheco, J., 1989. Cross-fault triggering in the November 1987  
914 Superstition Hills Earthquake Sequence, southern California. *Geophys. Res. Lett.* 16,  
915 199–202. <https://doi.org/10.1029/GL016i002p00199>

916 Jachens, R.C., Langenheim, V.E., Matti, J.C., 2002. Relationship of the 1999 Hector Mine and  
917 1992 Landers Fault Ruptures to Offsets on Neogene Faults and Distribution of Late  
918 Cenozoic Basins in the Eastern California Shear Zone. *Bull. Seismol. Soc. Am.* 92,  
919 1592–1605. <https://doi.org/10.1785/0120000915>

920 Ji, C., Wald, D.J., Helmberger, D.V., 2002. Source Description of the 1999 Hector Mine,  
921 California, Earthquake, Part I: Wavelet Domain Inversion Theory and Resolution  
922 Analysis. *Bull. Seismol. Soc. Am.* 92, 1192–1207. <https://doi.org/10.1785/0120000916>

923 Jin, Z., Fialko, Y.A., 2019. Rupture models of the 2019 M6.4-7.1 Ridgecrest earthquakes  
924 constrained by space geodetic data and aftershock locations. 1 Fall Meet. Abstr. 31.

925 Johnson, K.M., 2013. Slip rates and off-fault deformation in Southern California inferred from  
926 GPS data and models. *Journal of Geophysical Research: Solid Earth*, 118(10), pp.5643-  
927 5664.

928 Kaneko, Y., Fialko, Y., 2011. Shallow slip deficit due to large strike-slip earthquakes in dynamic  
929 rupture simulations with elasto-plastic off-fault response. *Geophys. J. Int.* 186, 1389–  
930 1403. <https://doi.org/10.1111/j.1365-246X.2011.05117>.

931 Kilb, D. and Rubin, A.M., 2002. Relocated microearthquakes of the Mt. Lewis ML5. 7,  
932 California, earthquake sequence: Implications of diverse fault orientations. *Journal of*  
933 *Geophysical Research*, 107, p.2294.

934 Kim, Y.-S., D.C. Peacock, and D.J. Sanderson, 2004, Fault damage zones, *J. Struct. Geol.*, 26,  
935 503-517.

936 Kreemer, C., Blewitt, G., Klein, E.C., 2014. A geodetic plate motion and Global Strain Rate  
937 Model. *Geochem. Geophys. Geosystems* 15, 3849–3889.  
938 <https://doi.org/10.1002/2014GC005407>

939 Lavrentiadis G, Abrahamson N. Generation of Surface-Slip Profiles in the Wavenumber  
940 Domain. *Bulletin of the Seismological Society of America*. 2019 Jun;109(3):888-907.

941 Li, Y. G., and J. E. Vidale (2001), Healing of the shallow fault zone from 1994–1998 after the  
942 1992 M7.5 Landers, California, earthquake, *Geophys. Res. Lett.*, 28, 2999–3002,  
943 doi:10.1029/2001GL012922.

944 Liu, C., Lay, T., Brodsky, E.E., Dascher-Cousineau, K., Xiong, X., 2019. Coseismic Rupture  
945 Process of the Large 2019 Ridgecrest Earthquakes From Joint Inversion of Geodetic and

946 Seismological Observations. *Geophys. Res. Lett.* 46, 11820–11829.  
947 <https://doi.org/10.1029/2019GL084949>

948 Marone, C.J., Scholtz, C.H., Bilham, R., 1991. On the mechanics of earthquake afterslip. *J.*  
949 *Geophys. Res. Solid Earth* 96, 8441–8452. <https://doi.org/10.1029/91JB00275>

950 McClusky, S.C., Bjornstad, S.C., Hager, B.H., King, R.W., Meade, B.J., Miller, M.M.,  
951 Monastero, F.C., Souter, B.J., 2001. Present day kinematics of the Eastern California  
952 Shear Zone from a geodetically constrained block model. *Geophys. Res. Lett.* 28, 3369–  
953 3372. <https://doi.org/10.1029/2001GL013091>

954 McGill, S.F., Wells, S.G., Fortner, S.K., Kuzma, H.A., McGill, J.D., 2009. Slip rate of the  
955 western Garlock fault, at Clark Wash, near Lone Tree Canyon, Mojave Desert,  
956 California Slip rate of the western Garlock fault. *GSA Bull.* 121, 536–554.  
957 <https://doi.org/10.1130/B26123.1>

958 McGuire, R.K., 1995. Probabilistic seismic hazard analysis and design earthquakes: Closing the  
959 loop. *Bull. Seismol. Soc. Am.* 85, 1275–1284.

960 McKenzie, D., Jackson, J., 1983. The relationship between strain rates, crustal thickening,  
961 palaeomagnetism, finite strain and fault movements within a deforming zone. *Earth*  
962 *Planet. Sci. Lett.* 65, 182–202. [https://doi.org/10.1016/0012-821X\(83\)90198-X](https://doi.org/10.1016/0012-821X(83)90198-X)

963 Meade, B.J., Hager, B.H., 2005. Block models of crustal motion in southern California  
964 constrained by GPS measurements. *J. Geophys. Res. Solid Earth* 110.  
965 <https://doi.org/10.1029/2004JB003209>

966 Miller, D.M. and Yount, J.C., 2002. Late Cenozoic tectonic evolution of the north-central Mojave  
967 Desert inferred from fault history and physiographic evolution of the Fort Irwin area,  
968 California. *Geologic evolution of the Mojave Desert and southwestern basin and range:*  
969 *Geological Society of America Memoir, 195*, pp.173-198.

970 Milliner, C.W.D., Dolan, J.F., Hollingsworth, J., Leprince, S., Ayoub, F., 2016. Comparison of  
971 coseismic near-field and off-fault surface deformation patterns of the 1992 Mw 7.3  
972 Landers and 1999 Mw 7.1 Hector Mine earthquakes: Implications for controls on the  
973 distribution of surface strain. *Geophys. Res. Lett.* 43, 10,115-10,124.  
974 <https://doi.org/10.1002/2016GL069841>



975 Mitchell, B.J., 1995. Anelastic structure and evolution of the continental crust and upper mantle  
976 from seismic surface wave attenuation. *Rev. Geophys.* 33, 441–462.  
977 <https://doi.org/10.1029/95RG02074>

978 Morelan, A.E. and Hernandez, J.L., 2020. Increasing Postearthquake Field Mapping Efficiency  
979 with Optical Image Correlation. *Bulletin of the Seismological Society of America.* 1–8,  
980 doi: 10.1785/0120200034

981 Murthy, K., Shearn, M., Smiley, B.D., Chau, A.H., Levine, J. and Robinson, M.D., 2014,  
982 October. SkySat-1: very high-resolution imagery from a small satellite. In *Sensors,*  
983 *Systems, and Next-Generation Satellites XVIII* (Vol. 9241, p. 92411E). International  
984 Society for Optics and Photonics.

985 Oskin, M., Perg, L., Shelef, E., Strane, M., Gurney, E., Singer, B., Zhang, X., 2008. Elevated  
986 shear zone loading rate during an earthquake cluster in eastern California. *Geology* 36,  
987 507–510. <https://doi.org/10.1130/G24814A.1>

988 Oskin, M. and Iriondo, A., 2004. Large-magnitude transient strain accumulation on the  
989 Blackwater fault, Eastern California shear zone. *Geology*, 32(4), pp.313-316.  
990 [doi.org/10.1130/G20223.1](https://doi.org/10.1130/G20223.1)

991 Ozacar, A.A., Beck, S.L., 2004. The 2002 Denali Fault and 2001 Kunlun Fault Earthquakes:  
992 Complex Rupture Processes of Two Large Strike-Slip Events. *Bull. Seismol. Soc. Am.*  
993 94, S278–S292. <https://doi.org/10.1785/0120040604>

994 Petersen, M.D., Dawson, T.E., Chen, R., Cao, T., Wills, C.J., Schwartz, D.P., Frankel, A.D.,  
995 2011. Fault Displacement Hazard for Strike-Slip Faults Displacement Hazard for Strike-  
996 Slip Faults. *Bull. Seismol. Soc. Am.* 101, 805–825. <https://doi.org/10.1785/0120100035>

997 Peyrat, S., Olsen, K., Madariaga, R., 2001. Dynamic modeling of the 1992 Landers earthquake.  
998 *J. Geophys. Res. Solid Earth* 106, 26467–26482. <https://doi.org/10.1029/2001JB000205>

999 Platt J. Persistent slip rate discrepancies in the eastern California (USA) shear zone: Comment.  
1000 *Geology.* 2017 Sep 1;45(9):e425-.

1001 Platt, J.P., Becker, T.W., 2013. Kinematics of rotating panels of E–W faults in the San Andreas  
1002 system: what can we tell from geodesy? *Geophys. J. Int.* 194, 1295–1301.  
1003 <https://doi.org/10.1093/gji/ggt189>

1004 Ponti, D.J., Blair, J.L., Rosa, C.M., K, T., Pickering, A.J., Morelan, A., Dawson, T., 2019.  
1005 Digital datasets documenting surface fault rupture and ground deformation features  
1006 produced by the Ridgecrest M6.4 and M7.1 earthquake sequence of July 4 and 5, 2019.  
1007 US Geol. Surv. Data Release. <https://doi.org/10.5066/P9BZ5IJ9>

1008 Ramsay, J.G., 1967. Folding And Fracturing Of Rocks. McGraw-Hill Book Company, New  
1009 York p. 568.

1010 Rice, J.R., 1975. On the stability of dilatant hardening for saturated rock masses. *J. Geophys.*  
1011 *Res.* 1896-1977 80, 1531–1536. <https://doi.org/10.1029/JB080i011p01531>

1012 Rockwell, T.K., Lindvall, S., Dawson, T., Langridge, R., Lettis, W., Klinger, Y., 2002. Lateral  
1013 Offsets on Surveyed Cultural Features Resulting from the 1999 İzmit and Düzce  
1014 Earthquakes, Turkey. *Bull. Seismol. Soc. Am.* 92, 79–94.  
1015 <https://doi.org/10.1785/0120000809>

1016 Rockwell, T.K., Lindvall, S., Herzberg, M., Murbach, D., Dawson, T., Berger, G., 2000.  
1017 Paleoseismology of the Johnson Valley, Kickapoo, and Homestead Valley Faults:  
1018 Clustering of Earthquakes in the Eastern California Shear Zone. *Bull. Seismol. Soc. Am.*  
1019 90, 1200–1236. <https://doi.org/10.1785/0119990023>

1020 Ron, H., Freund, R., Garfunkel, Z., Nur, A., 1984. Block rotation by strike-slip faulting:  
1021 Structural and paleomagnetic evidence. *J. Geophys. Res. Solid Earth* 89, 6256–6270.  
1022 <https://doi.org/10.1029/JB089iB07p06256>

1023 Rousseau, C.E. and Rosakis, A.J., 2003. On the influence of fault bends on the growth of sub-  
1024 Rayleigh and intersonic dynamic shear ruptures. *Journal of Geophysical Research: Solid*  
1025 *Earth*, 108(B9).

1026 Ross, Z.E., Idini, B., Jia, Z., Stephenson, O.L., Zhong, M., Wang, X., Zhan, Z., Simons, M.,  
1027 Fielding, E.J., Yun, S.-H., Hauksson, E., Moore, A.W., Liu, Z., Jung, J., 2019.  
1028 Hierarchical interlocked orthogonal faulting in the 2019 Ridgecrest earthquake sequence.  
1029 *Science* 366, 346–351. <https://doi.org/10.1126/science.aaz0109>

1030 Sammis, C.G., Rosakis, A.J., Bhat, H.S., 2010. Effects of Off-fault Damage on Earthquake  
1031 Rupture Propagation: Experimental Studies, in: Ben-Zion, Y., Sammis, C. (Eds.),  
1032 Mechanics, Structure and Evolution of Fault Zones, Pageoph Topical Volumes.  
1033 Birkhäuser, Basel, pp. 1629–1648. [https://doi.org/10.1007/978-3-0346-0138-2\\_5](https://doi.org/10.1007/978-3-0346-0138-2_5)

1034 Savage, J.C., Burford, R.O., 1973. Geodetic determination of relative plate motion in central  
1035 California. *J. Geophys. Res.* 1896-1977 78, 832–845.  
1036 <https://doi.org/10.1029/JB078i005p00832>

1037 Savage, J.C., Gan, W., Svarc, J.L., 2001. Strain accumulation and rotation in the Eastern  
1038 California Shear Zone. *J. Geophys. Res. Solid Earth* 106, 21995–22007.  
1039 <https://doi.org/10.1029/2000JB000127>

1040 Savage, J.C., Svarc, J.L. and Prescott, W.H., 2004. Interseismic strain and rotation rates in the  
1041 northeast Mojave domain, eastern California. *Journal of Geophysical Research: Solid*  
1042 *Earth*, 109(B2). <https://doi.org/10.1029/2003JB002705>

1043 Scharer, K.M., Salisbury, J.B., Arrowsmith, J.R., Rockwell, T.K., 2014. Southern San Andreas  
1044 Fault Evaluation Field Activity: Approaches to Measuring Small Geomorphic Offsets—  
1045 Challenges and Recommendations for Active Fault Studies. *Seismol. Res. Lett.* 85, 68–  
1046 76. <https://doi.org/10.1785/0220130108>

1047 Schermer, E.R., Luyendyk, B.P. and Cisowski, S., 1996. Late Cenozoic structure and tectonics of  
1048 the northern Mojave Desert. *Tectonics*, 15(5), pp.905-932.

1049 Scholz, C.H., 2019. *The mechanics of earthquakes and faulting*. Cambridge university press.

1050 Scott, C.P., Arrowsmith, J.R., Nissen, E., Lajoie, L., Maruyama, T., Chiba, T., 2018. The M7  
1051 2016 Kumamoto, Japan, Earthquake: 3-D Deformation Along the Fault and Within the  
1052 Damage Zone Constrained From Differential Lidar Topography. *J. Geophys. Res. Solid*  
1053 *Earth* 123, 6138–6155. <https://doi.org/10.1029/2018JB015581>

1054 Shelef, E., Oskin, M., 2010. Deformation processes adjacent to active faults: Examples from  
1055 eastern California. *J. Geophys. Res. Solid Earth* 115.  
1056 <https://doi.org/10.1029/2009JB006289>

1057 Shi Z, Day SM., 2013, Rupture dynamics and ground motion from 3-D rough-fault simulations.  
1058 *Journal of Geophysical Research: Solid Earth*. Mar;118(3):1122-41.

1059 Sieh, K., Jones, L., Hauksson, E., Hudnut, K., Eberhart-Phillips, D., Heaton, T., Hough, S.,  
1060 Hutton, K., Kanamori, H., Lilje, A. and Lindvall, S., 1993. Near-field investigations of  
1061 the Landers earthquake sequence, April to July 1992. *Science*, 260(5105), pp.171-176.

1062 Smith, K., Hatch, R. L., Ruhl, C. J., & Abercrombie, R. E. (2020, 08). Order and timing of high-  
1063 angle conjugate strike-slip faulting in Walker Lane sequences. Poster Presentation at  
1064 2020 SCEC Annual Meeting.

1065 Socquet, A., Hollingsworth, J., Pathier, E., Bouchon, M., 2019. Evidence of supershear during  
1066 the 2018 magnitude 7.5 Palu earthquake from space geodesy. *Nat. Geosci.* 12, 192–199.  
1067 <https://doi.org/10.1038/s41561-018-0296-0>

1068 Stirling MW, Wesnousky SG, Shimazaki K. Fault trace complexity, cumulative slip, and the  
1069 shape of the magnitude-frequency distribution for strike-slip faults: A global survey.  
1070 *Geophysical Journal International*. 1996 Mar 1;124(3):833-68.

1071 Tchalenko JS. Similarities between shear zones of different magnitudes. *Geological Society of*  
1072 *America Bulletin*. 1970 Jun 1;81(6):1625-40.

1073 Teran, O.J., Fletcher, J.M., Oskin, M.E., Rockwell, T.K., Hudnut, K.W., Spelz, R.M., Akciz,  
1074 S.O., Hernandez-Flores, A.P., Morelan, A.E., 2015. Geologic and structural controls on  
1075 rupture zone fabric: A field-based study of the 2010 Mw 7.2 El Mayor–Cucapah  
1076 earthquake surface rupture. *Geosphere* 11, 899–920. <https://doi.org/10.1130/GES01078.1>

1077 Thomas, M.Y., Bhat, H.S., 2018. Dynamic evolution of off-fault medium during an earthquake:  
1078 a micromechanics based model. *Geophys. J. Int.* 214, 1267–1280.  
1079 <https://doi.org/10.1093/gji/ggy129>

1080 U.S. Geological Survey and California Geological Survey, Quaternary fault and fold database for  
1081 the United States, accessed March 1 2020, at: [https://www.usgs.gov/natural-](https://www.usgs.gov/natural-hazards/earthquake-hazards/faults)  
1082 [hazards/earthquake-hazards/faults](https://www.usgs.gov/natural-hazards/earthquake-hazards/faults).

1083 Vidale JE, Li YG. Damage to the shallow Landers fault from the nearby Hector Mine  
1084 earthquake. 2003, *Nature* Jan;421(6922):524-6.

1085 Wang, K., Dreger, D. S., Tinti, E., Bürgmann, R., and Taira, T., 2020, Rupture process of the  
1086 2019 Ridgecrest, California M6.4 Foreshock and M7.1 Earthquake Constrained by  
1087 Seismic and Geodetic Data, *Bull. Seismol. Soc. Am.* 92,  
1088 <https://doi.org/10.1785/0120200108>

1089 Wesnousky, S.G., 1988. Seismological and structural evolution of strike-slip  
1090 faults. *Nature*, 335(6188), pp.340-343.

1091 Wesnousky, S.G., 2005. The San Andreas and Walker Lane fault systems, western North  
1092 America: transpression, transtension, cumulative slip and the structural evolution of a  
1093 major transform plate boundary. *J. Struct. Geol.* 27, 1505–1512.  
1094 <https://doi.org/10.1016/j.jsg.2005.01.015>

1095 Willis, MJ; Barnhart, WD; Cassotto, R; Klassen, J; Corcoran, J; Host, T; Huberty, B., Pelletier, K.,  
1096 Knight, J.F., *CaliDEM: Ridgecrest, CA Region 2m Digital Surface Elevation Model*. Funding  
1097 by NSF and USGS. Data collection by DigitalGlobe. Distributed by OpenTopography.  
1098 <https://doi.org/10.5069/G998854C>

1099 Xu, S., and Y. Ben-Zion, 2013, Numerical and theoretical analyses of in-plane dynamic rupture  
1100 on a frictional interface and off-fault yielding patterns at different scales: *Geophys. J.*  
1101 *Int.*, 193, 304-320.

1102 Xu, X., Sandwell, D.T., Smith-Konter, B., 2020. Coseismic Displacements and Surface Fractures  
1103 from Sentinel-1 InSAR: 2019 Ridgecrest Earthquakes. *Seismol. Res. Lett.*  
1104 <https://doi.org/10.1785/0220190275>

1105 Xu, X., Tong, X., Sandwell, D.T., Milliner, C.W.D., Dolan, J.F., Hollingsworth, J., Leprince, S.,  
1106 Ayoub, F., 2016. Refining the shallow slip deficit. *Geophys. J. Int.* 204, 1867–1886.  
1107 <https://doi.org/10.1093/gji/ggv563>

1108 Zinke, R., Hollingsworth, J. and Dolan, J.F., 2014. Surface slip and off-fault deformation  
1109 patterns in the 2013 MW 7.7 Balochistan, Pakistan earthquake: Implications for controls  
1110 on the distribution of near-surface coseismic slip. *Geochemistry, Geophysics,*  
1111 *Geosystems*, 15(12), pp.5034-5050.

1112 Zhou, Y., Parsons, B.E., Walker, R.T., 2018. Characterizing Complex Surface Ruptures in the  
1113 2013 Mw 7.7 Balochistan Earthquake Using Three-Dimensional Displacements. *J.*  
1114 *Geophys. Res. Solid Earth* 123, 10,191-10,211. <https://doi.org/10.1029/2018JB016043>

1115  
1116  
1117  
1118  
1119  
1120  
1121

1122 **Table 1** Summary of statistics and values estimated for the foreshock fault rupture that includes  
1123 comparisons of observed and predicted values for the bookshelf slip model.

1124

	<b>Observed</b>	<b>Predicted</b>
<b>Dextral slip (<math>\gamma</math>, meter)</b>	0.98	-

<b>Angle between faults (<math>\alpha</math>, °)</b>	86	-
<b>Sinistral slip (<math>\gamma'</math>, meter)</b>	0.71–1.4	0.97
<b>Cumulative displacement (<math>d_{fore}</math>)</b>	256-600	-
<b>Total long-term block rotation (<math>\omega_T</math>, °)</b>	3-7	-
<b>Mean displacement (<math>d</math>, meter)</b>	0.71	-
<b>Maximum displacement, (meter)</b>	1.4	-
<b>Median off-fault deformation (OFD, %)</b>	65	-
<b>Mean off-fault deformation (OFD, %)</b>	56	-
<b>Mean Fault zone width</b>	59	-
<b>Shallow slip deficit (%)</b>	42-65*	-

\*(Chen et al., 2020; Jin & Fialko, 2020; Wang et al., 2020; Xu et al., 2020)

1125  
1126  
1127  
1128  
1129  
1130

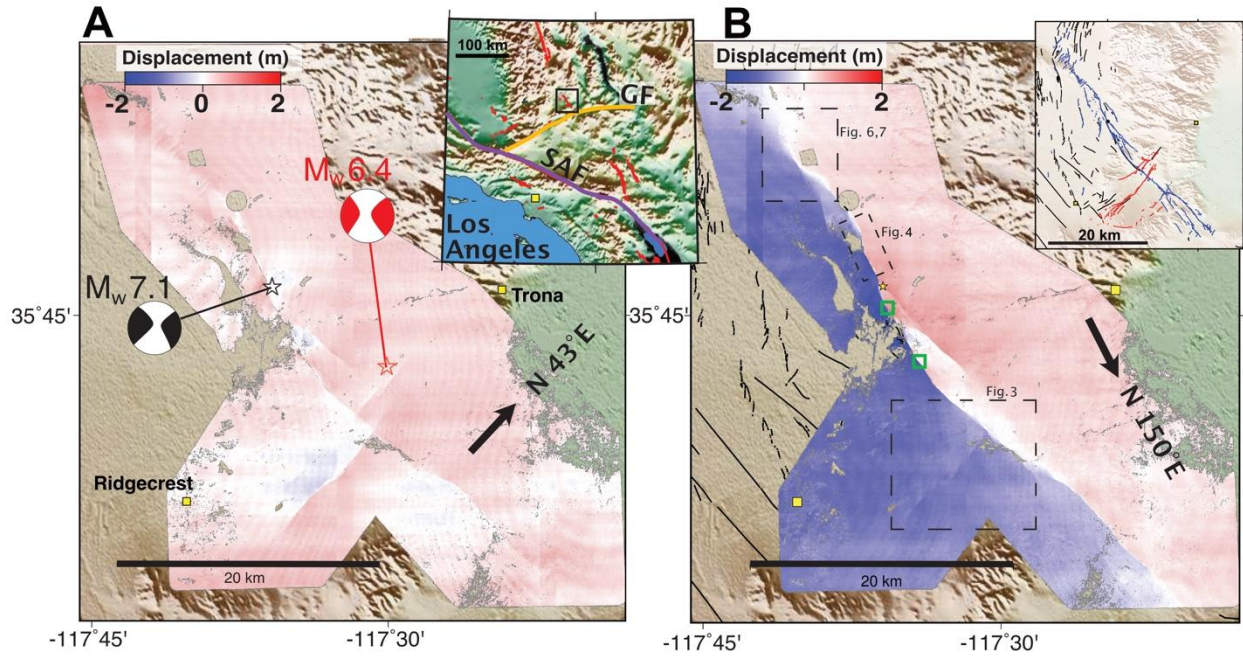
**Table 2** Summary of statistics and values estimated for the mainshock fault rupture that includes comparison of observed and predicted values for the bookshelf slip model.

	<b>Observed</b>	<b>Predicted</b>
<b>Dextral slip (<math>\gamma</math>, meter)</b>	1.6	-
<b>Angle between faults (<math>\alpha</math>, °)</b>	66	-
<b>Sinistral slip (<math>\gamma'</math>, meter)</b>	0.8	1
<b>Instantaneous block rotation (<math>\omega</math>, °)</b>	0.06	0.05
<b>Internal block strain (<math>e</math>, %)</b>	0.004	0.0044
<b>Mean displacement (<math>d</math>, meter)</b>	1.69	-
<b>Macroscopic block width (<math>w_b</math>, meter)</b>	4,890	
<b>Median off-fault deformation (OFD, %)</b>	25	-
<b>Mean off-fault deformation (OFD, %)</b>	34	-
<b>Mean Fault zone width ( fault zone width, meter)</b>	69	-
<b>Shallow slip deficit (%)</b>	18-35*	-

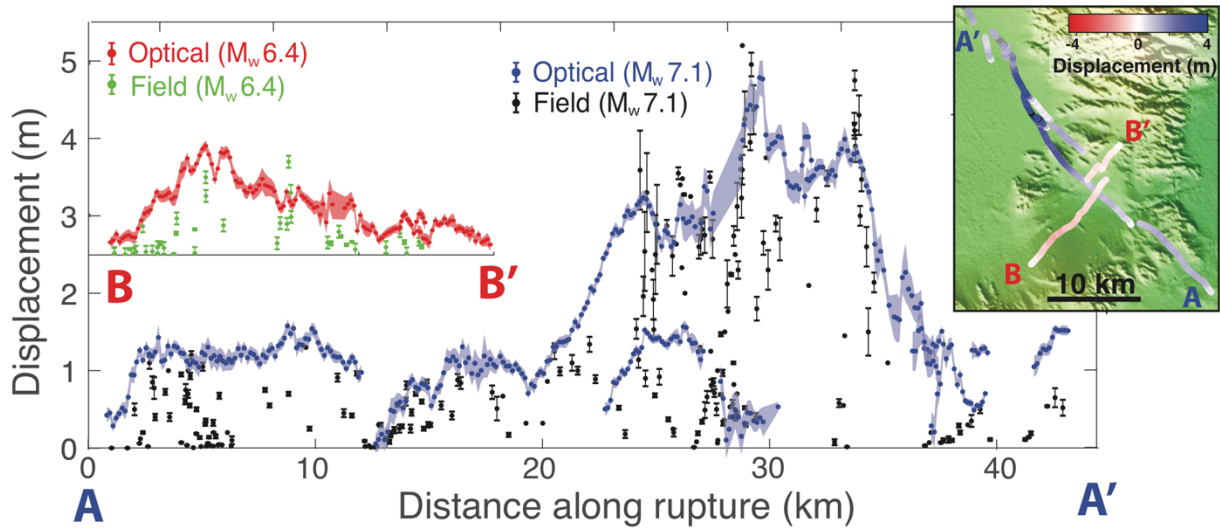
\*(Chen et al., 2020; Jin & Fialko, 2020; Wang et al., 2020; Xu et al., 2020)

1131  
1132  
1133  
1134

1135  
1136 **Figures**  
1137



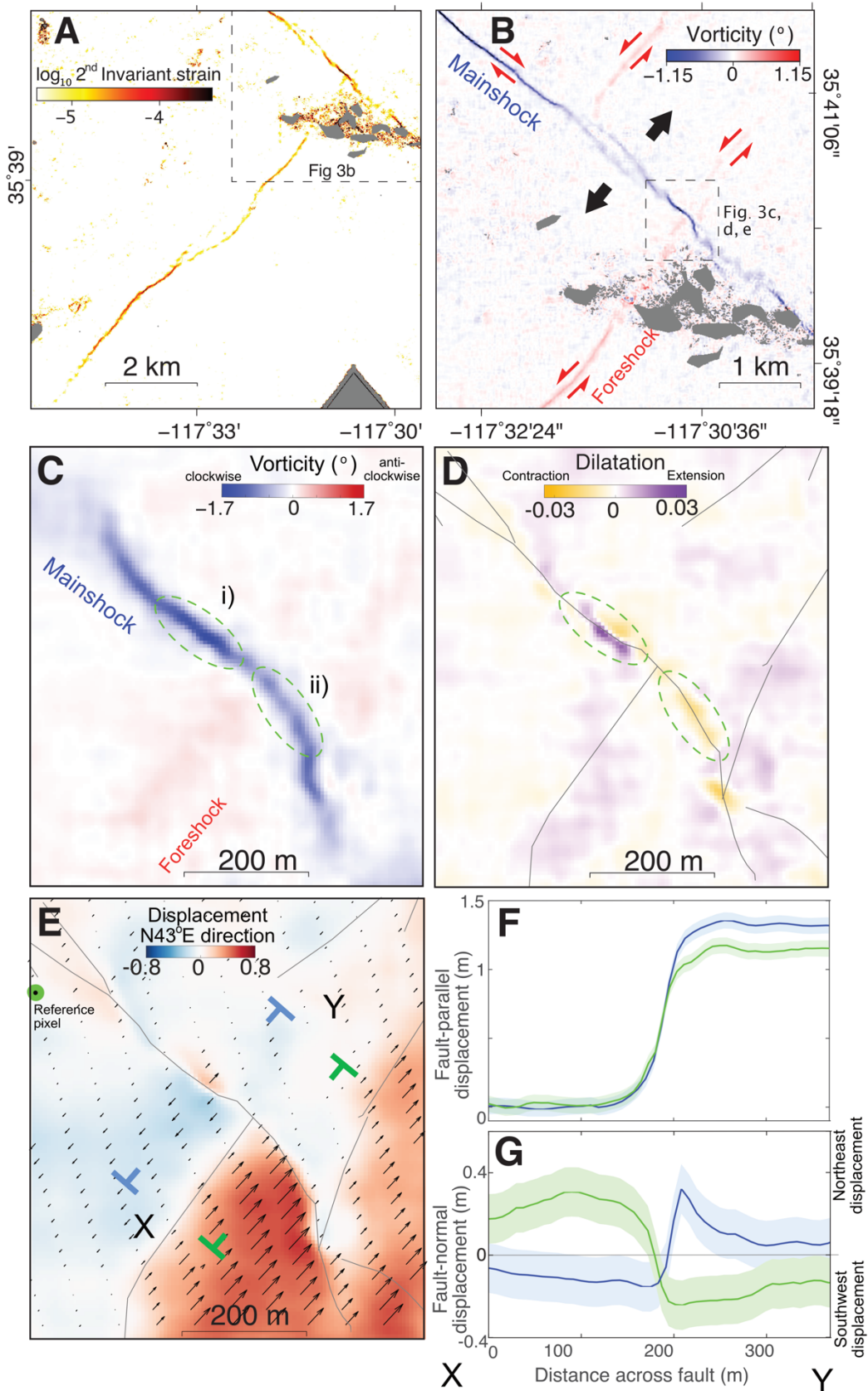
1138  
1139 **Figure 1. Displacement maps from optical image correlation that measures surface motion**  
1140 **from both the foreshock (July 4<sup>th</sup>, 2019) and mainshock ruptures (July 6<sup>th</sup>, 2019).** The pre-  
1141 event image was acquired on September 15th, 2018 and the post image on July 24th, 2019 and  
1142 therefore surface motion from both events are found within the surface displacement maps. A)  
1143 Displacement projected into the N43°E direction parallel to foreshock faults. Inset shows the  
1144 location of Ridgecrest region (black rectangle), San Andreas fault (SAF, purple line) and Garlock  
1145 fault (GF, orange line). B) Displacement projected into the N150°E direction, parallel to mainshock  
1146 faults. Focal mechanisms from CMT catalogue. (Dziewonski et al., 1981; Ekström et al., 2012).  
1147 Inset in upper right shows fault rupture traces of the foreshock (red) and mainshock (blue) mapped  
1148 from field surveys (Ponti et al., 2019), with black lines showing Quaternary mapped faults (USGS,  
1149 2020). Green boxes along central segment of rupture show the location of transpressional bends.  
1150



1151  
 1152  
 1153  
 1154  
 1155  
 1156  
 1157  
 1158  
 1159  
 1160  
 1161  
 1162  
 1163

**Figure 2. Comparison of slip profiles of the foreshock and mainshock events made from field and optical measurements.** Slip along the foreshock is measured along three parallel fault strands and slip along the mainshock is measured along eight. Red and green values show optical and field measurements along the foreshock rupture, respectively, and blue and black are optical and field measurements along the mainshock, respectively. Optical displacements capture the total displacement across the surface rupture using profiles with  $> 0.5$  km in across-fault length (e.g., Figure S1), which includes both on-fault displacement and off-fault distributed inelastic strain, explaining why the majority are larger than the field displacement measurements from Ponti et al. (2019). Inset in top right shows the same optical displacement measurements in map view.

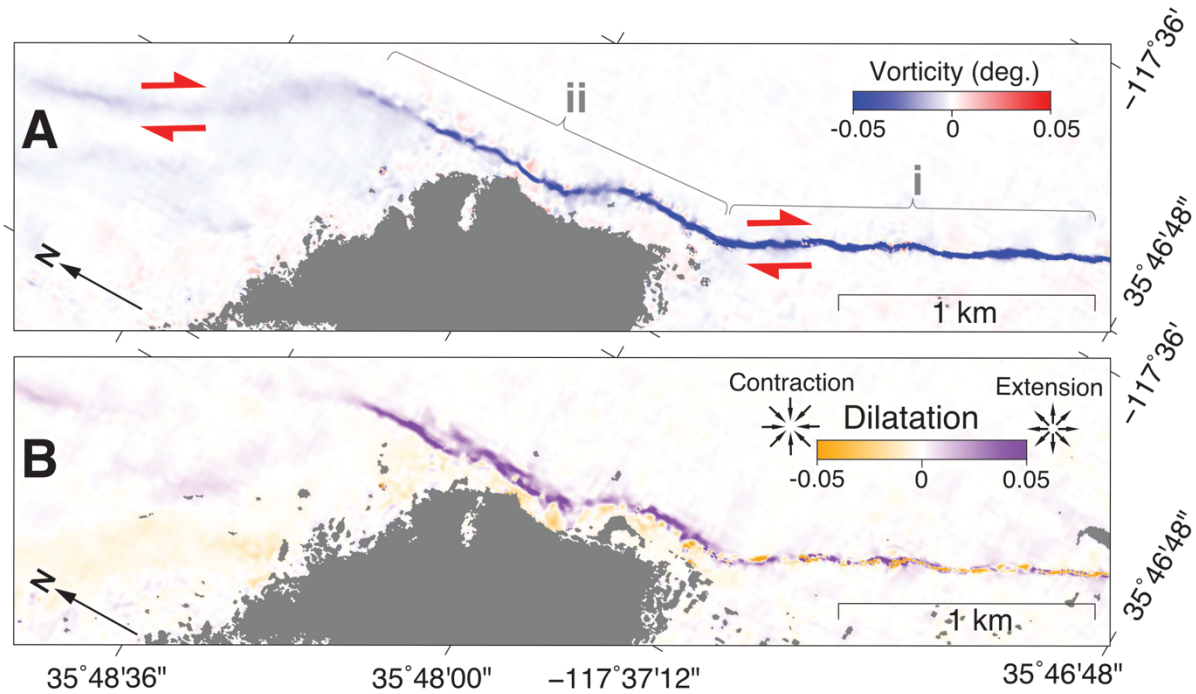




1165 **Figure 3. Strain maps of the foreshock-mainshock intersection region illustrating how strain**  
1166 **release along the mainshock was affected by the foreshock rupture.** a) Logarithm of  $I_2$ , which  
1167 illustrates how the scalar strain intensity varies along the rupture. b) Vorticity map illustrating the  
1168 different shear senses around the mainshock-foreshock intersection. c) Zoom of vorticity map  
1169 illustrating an increase along segment i) and lower values along segment ii), suggesting a possible  
1170 difference in the intensity of simple shear strain. d) Dilatation of the intersection region  
1171 highlighting how different segments experienced contraction (orange) and extension (purple) due  
1172 to imposed stress changes from the foreshock rupture. Gray lines show major fault traces from  
1173 field mapping (Ponti et al., 2019). e) Surface displacement projected into the NE direction,  
1174 illustrating motion perpendicular to the mainshock rupture shown both by the colors (amplitude of  
1175 motion) and the vectors. This shows clear extension across the blue profile (vectors diverging away  
1176 from each across the mainshock rupture) and contraction across the green profile (shown by  
1177 vectors converging across the mainshock rupture, profiles labelled X-Y). f) and g) show surface  
1178 motion that is projected in the direction parallel to and perpendicular to the strike of the mainshock  
1179 rupture, respectively, along profiles located between X and Y.

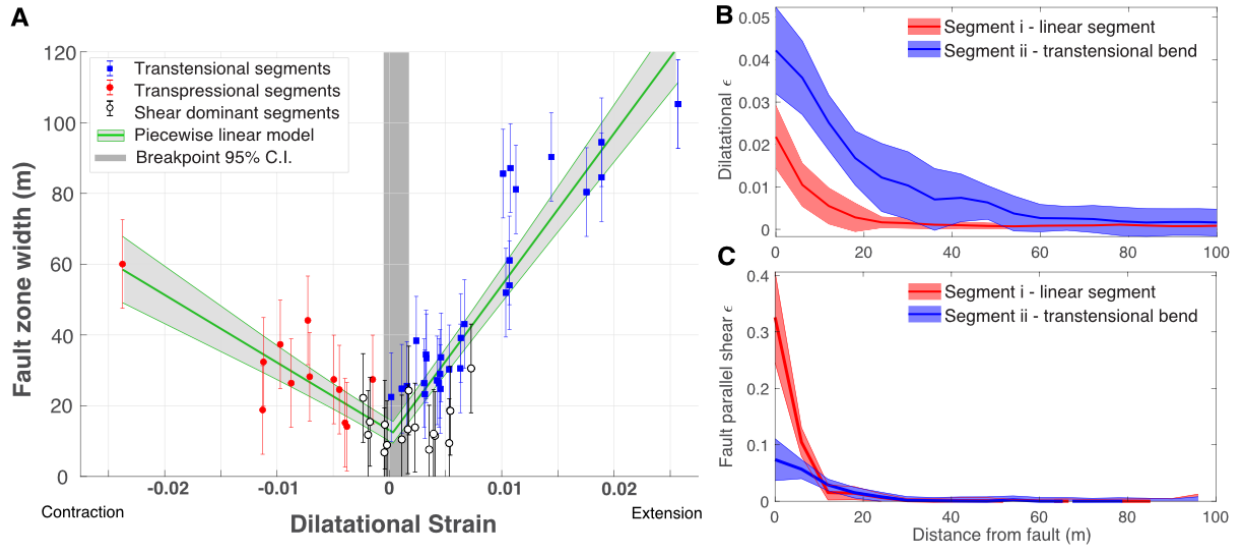
1180

1181

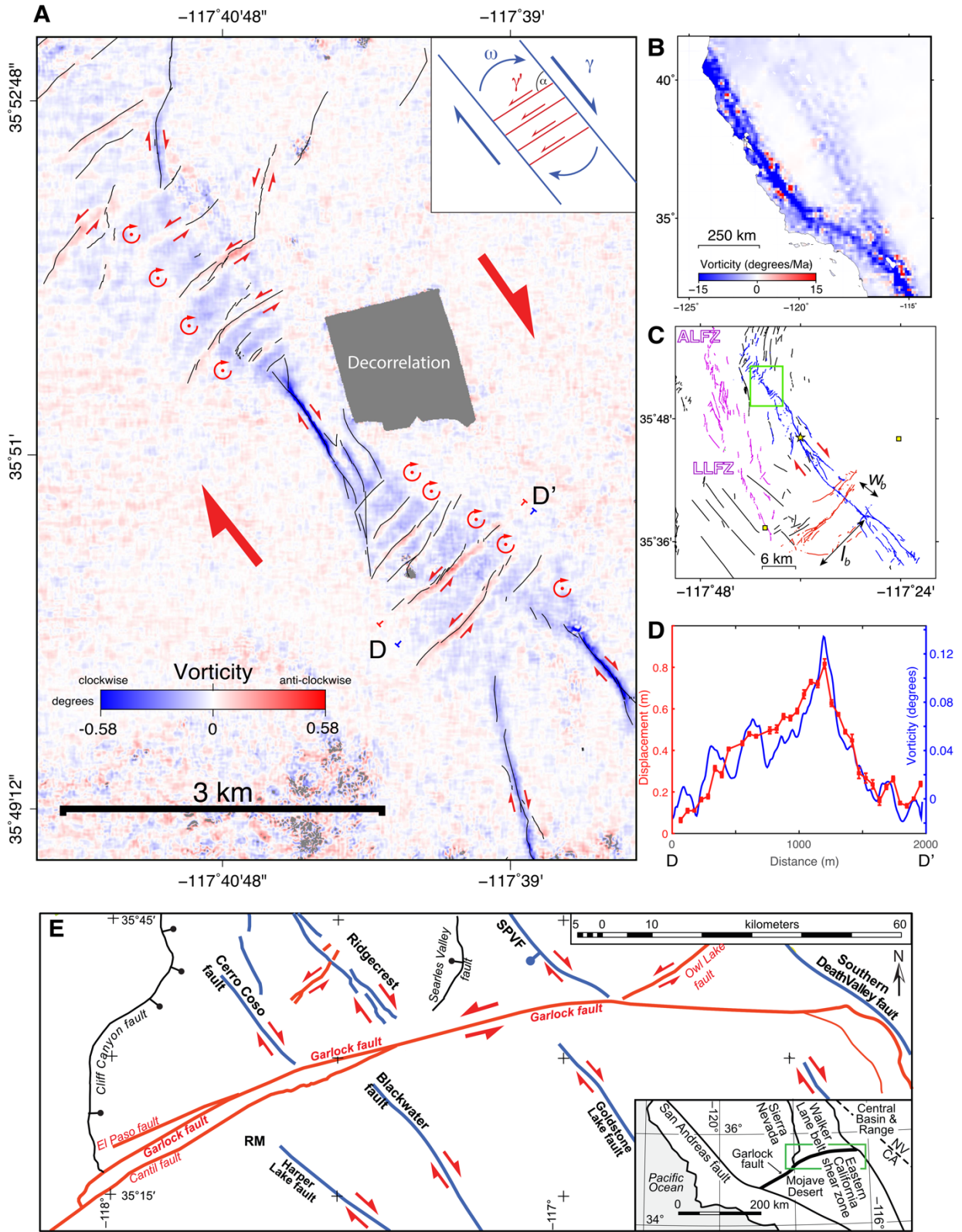


1182  
 1183 **Figure 4. Strain maps along a transtensional bend.** A) Vorticity along a transtensional bend  
 1184 located near the northern end of the mainshock rupture (see Figure 1 for location), segments i and  
 1185 ii show location of profiles used in Fig. 4b and c. B) Dilatational strain component along the  
 1186 transtensional bend showing systematic variations of width between the bend and adjacent linear  
 1187 segment, and variations of the type of dilatation according to subtle curvature of the fault along  
 1188 segment i. See Figure 1 for locations. Gray area is region of decorrelation due to changing playa  
 1189 surface.

1190

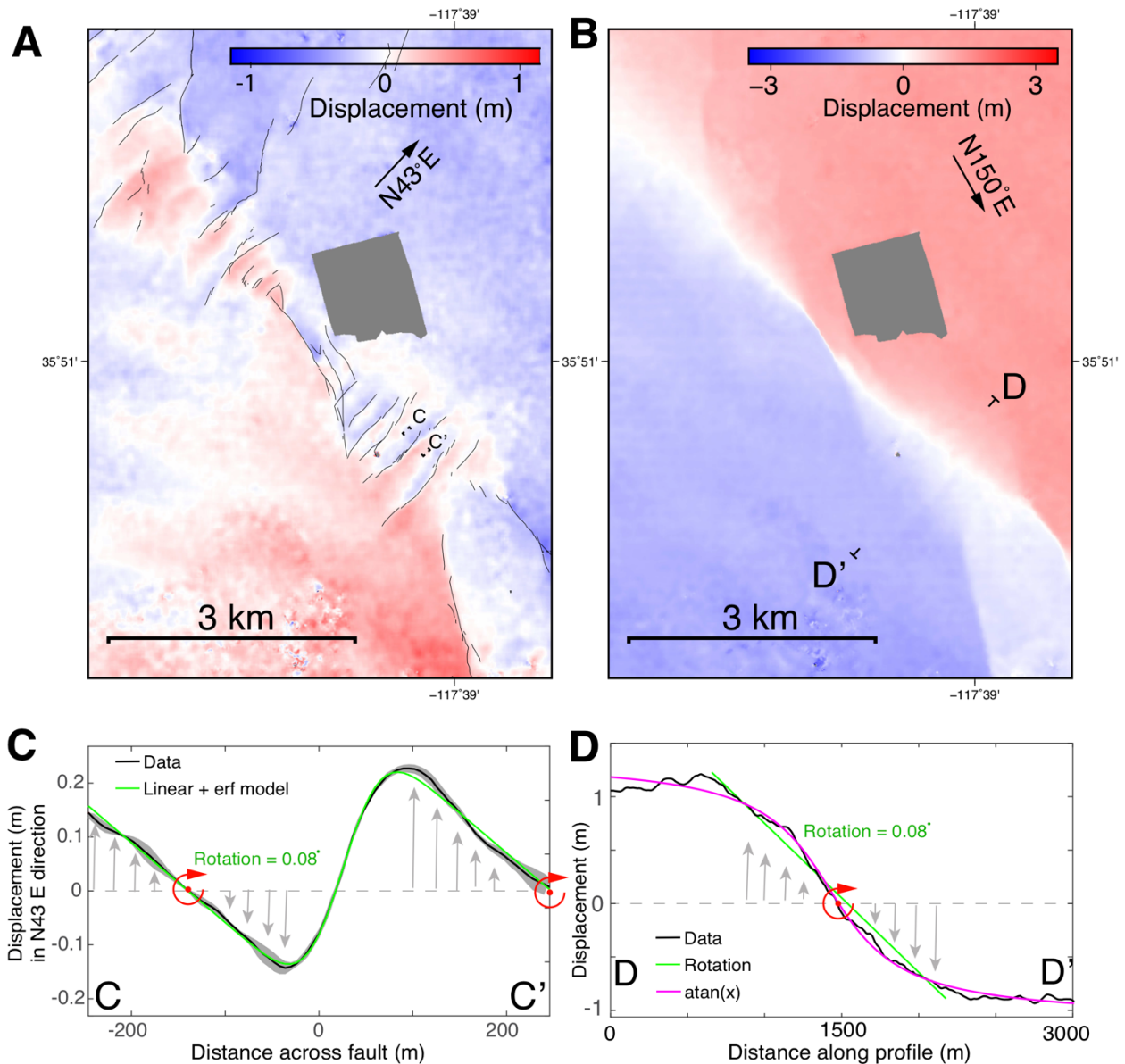


1191  
 1192 **Figure 5. Variation of fault zone width with dilatational strain.** A) Fault width measured  
 1193 from three different strain regimes, contractional (red), shear dominated (white), and extensional  
 1194 (blue), which shows that a segmented piecewise linear function can explain the variation, with  
 1195 wider fault zones with increasing amounts of dilatational strain. Dark vertical gray band is 95%  
 1196 confidence interval of the breakpoint estimated by bootstrapping the data with 3000 simulations.  
 1197 Light gray bands are 95% confidence intervals of the segmented regression. B) shows the decay  
 1198 of inelastic strain from strain profiles taken across the transtensional bend (segment ii) from the  
 1199 dilatation map shown in Fig. 4b, where dilatational strain is significantly wider along the  
 1200 transtensional bend than the adjacent segment (segment i) that experiences mostly shear strain. C)  
 1201 shows fault-parallel shear strain, with high-strain fault core along segment i and lower shear strains  
 1202 in ii.



1204 **Figure 6. Vorticity of the vector field illustrating bookshelf faulting and rotations associated**  
1205 **with simple shear.** Location is shown as the green box in c) and Figure 1. A) Positive (negative)  
1206 colors show anti-clockwise (clockwise) rotation in a right-handed coordinate system. Black lines  
1207 are faults mapped in the field (Ponti et al., 2019). The vorticity illustrates that strain beyond the  
1208 fault tips of dextral faults transition to rotation, where according to field mapping (black lines)  
1209 fracturing is only limited to larger, finite amounts of strain, suggesting rotation accommodates  
1210 lower strains between faults. Inset shows schematic illustrating the kinematics of bookshelf slip  
1211 model consisting of regional dextral displacement (blue lines,  $\gamma$ ), rotation of blocks ( $\omega$ ), rotation  
1212 of sinistral oblique fault ( $\alpha$ ), and slip on oblique faults (red,  $\gamma'$ ), modified from Platt & Becker  
1213 (2013). B) Vorticity rate from GPS velocities along the North America-Pacific plate boundary,  
1214 blue is clockwise, red anticlockwise from Kremer et al. (2014). C) Fault traces of the foreshock  
1215 rupture (red), mainshock (blue) and Little Lake and Airport Fault Zones (LLFZ, ALFZ, magenta),  
1216 illustrating the larger scale ‘bookshelf’ with block width ( $w_b$ ). D) Profile of vorticity and  
1217 displacement along and adjacent to the second southernmost sinistral fault (note displacement is  
1218 measured from displacement map shown in Fig. 6b), where a non-constant vorticity and slip is  
1219 evidence of non-rigid block strain. E) Map view of NW-trending dextral faults of the ECSZ show  
1220 that they do not intersect with the sinistral WSW-trending Garlock fault, which could be explained  
1221 by clockwise block rotation beyond the tips of dextral faults similar to that found in a), figure  
1222 adapted from Andrew et al. (2015).  
1223

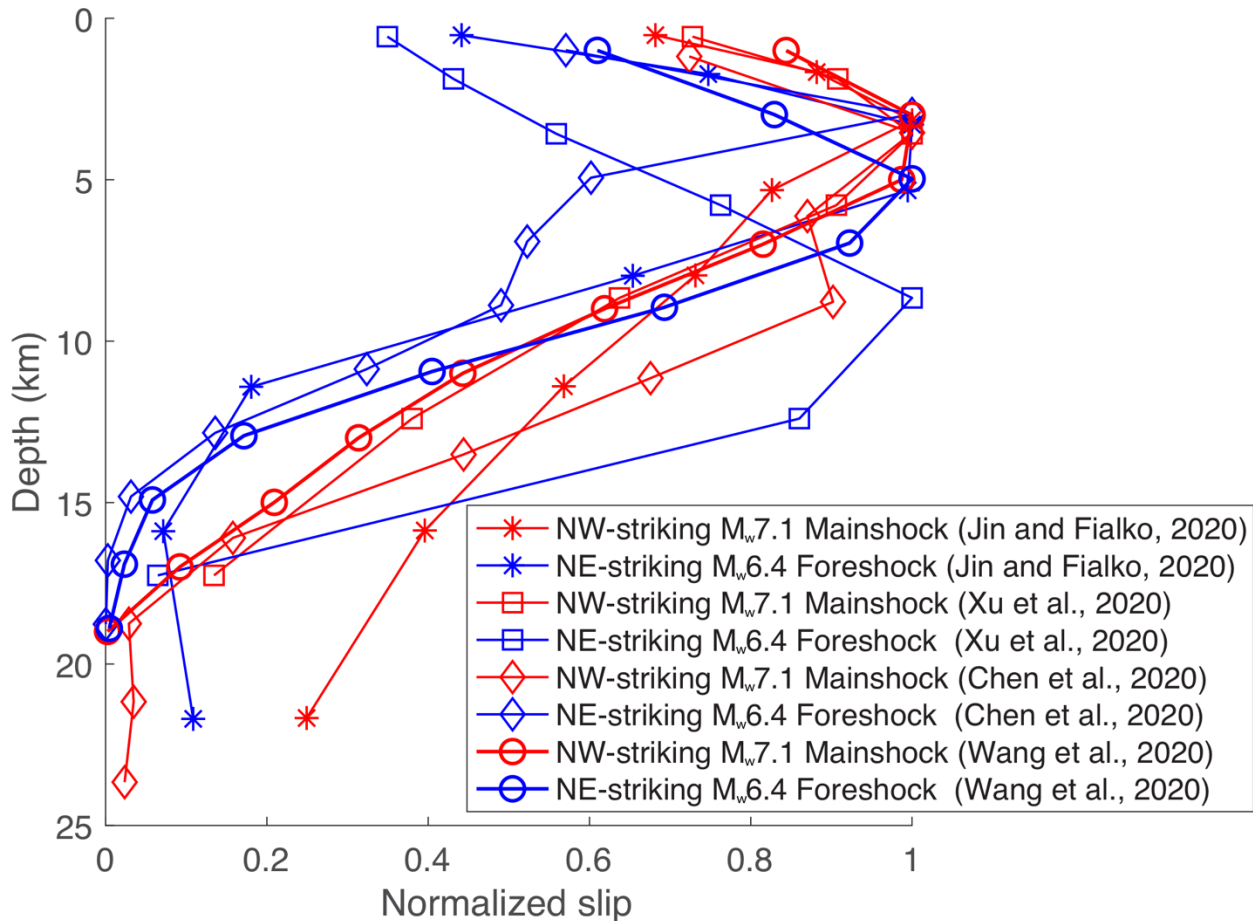




1224  
 1225 **Figure 7. Projected surface displacement illustrating bookshelf kinematics.** Location shown  
 1226 in Figure 1. A) shows displacement projected into NE that highlights motion along the oblique NE  
 1227 trending sinistral faults and contraction of dextral faults, while b) shows displacement projected  
 1228 into SE direction parallel to the NW-trending dextral faults illustrating distributed shear across the  
 1229 bookshelf. C) shows profile of displacement from a) normal to one of the sinistral oblique faults  
 1230 illustrating rotation of displacement discontinuities (location is shown in panel A between the  
 1231 labels C-C'). D) shows that distributed shear across the bookshelf is not well explained by constant  
 1232 motion (green line) indicative of rigid-block rotation, but instead by shear that increases towards  
 1233 the center of the 'bookshelf' described by an arctan function from a screw dislocation model  
 1234 (location of profile is shown in b), between labels D and D'). Inverting the surface motion (black

1235 line) suggests a possible single, freely slipping, discrete fault that reaches from depth to 342 m  
1236 below the surface (magenta line).





1237  
 1238  
 1239  
 1240  
 1241  
 1242  
 1243  
 1244  
 1245  
 1246  
 1247  
 1248

**Figure 8. Normalized slip depth distributions for the  $M_w$  6.4 foreshock (blue) and the  $M_w$  7.1 mainshock (red) from different slip inversions.** Here we have assumed that the  $M_w$  6.4 foreshock rupture was mainly along the NE-striking sinistral fault segments, whereas the  $M_w$  7.1 mainshock rupture was along the NW-striking dextral faults, although seismicity and inversion of seismic and geodetic data suggest that the  $M_w$  6.4 foreshock may involve rupturing along the NW-striking faults too (Ross et al., 2019; Chen et al., 2020; Wang et al., 2020). Despite large variations among these models they all systematically show that the foreshock had a higher shallow slip deficit ranging from 42-65% while the mainshock ranges from 18-35% (Chen et al., 2020; Jin and Fialko, 2020; Wang et al., 2020; Xu et al., 2020).